NOTE TO USERS

Page(s) not included in the original manuscript and are unavailable from the author or university. The manuscript was scanned as received.

77-83

This reproduction is the best copy available.

UMI®

uOttawa

L'Université canadienne
Canada's university

**FACULTÉ DES ÉTUDES SUPÉRIEURES
ET POSTOCTORALES**

uOttawa

L'Université canadienne
Canada's university

**FACULTY OF GRADUATE AND
POSDOCTORAL STUDIES**

Mehran Talebinejad
AUTEUR DE LA THÈSE / AUTHOR OF THESIS

M.A.Sc. (Electrical Engineering)
GRADE / DEGREE

School of Information Technology and Engineering
FACULTÉ, ÉCOLE, DÉPARTEMENT / FACULTY, SCHOOL, DEPARTMENT

Fractal Analysis of Myoelectric Signals
TITRE DE LA THÈSE / TITLE OF THESIS

Ali Miri
DIRECTEUR (DIRECTRICE) DE LA THÈSE / THESIS SUPERVISOR

Adrian Chan
CO-DIRECTEUR (CO-DIRECTRICE) DE LA THÈSE / THESIS CO-SUPERVISOR

EXAMINATEURS (EXAMINATRICES) DE LA THÈSE / THESIS EXAMINERS

Richard Dansereau

Andy Adler

Gary W. Slater
LE DOYEN DE LA FACULTÉ DES ÉTUDES SUPÉRIEURES ET POSTDOCTORALES /
DEAN OF THE FACULTY OF GRADUATE AND POSTDOCORAL STUDIES

FRACTAL ANALYSIS OF MYOELECTRIC SIGNALS

A THESIS SUBMITTED TO
THE FACULTY OF GRADUATE AND POSTDOCTORAL STUDIES
IN PARTIAL FULFILLMENT OF THE REQUIRMENTS
FOR THE DEGREE OF
MASTER OF APPLIED SCIENCE

OTTAWA-CARLETON INSTITUTE FOR ELECTRICAL AND COMPUTER ENGINEERING
SCHOOL OF INFORMATION TECHNOLOGY AND ENGINEERING
UNIVERSITY OF OTTAWA

MEHRAN TALEBINEJAD
APRIL 2006

Library and
Archives Canada

Published Heritage
Branch

395 Wellington Street
Ottawa ON K1A 0N4
Canada

Bibliothèque et
Archives Canada

Direction du
Patrimoine de l'édition

395, rue Wellington
Ottawa ON K1A 0N4
Canada

Your file Votre référence
ISBN: 978-0-494-14957-7
Our file Notre référence
ISBN: 978-0-494-14957-7

NOTICE:
The author has granted a non-exclusive license allowing Library and Archives Canada to reproduce, publish, archive, preserve, conserve, communicate to the public by telecommunication or on the Internet, loan, distribute and sell theses worldwide, for commercial or non-commercial purposes, in microform, paper, electronic and/or any other formats.

The author retains copyright ownership and moral rights in this thesis. Neither the thesis nor substantial extracts from it may be printed or otherwise reproduced without the author's permission.

AVIS:
L'auteur a accordé une licence non exclusive permettant à la Bibliothèque et Archives Canada de reproduire, publier, archiver, sauvegarder, conserver, transmettre au public par télécommunication ou par l'Internet, prêter, distribuer et vendre des thèses partout dans le monde, à des fins commerciales ou autres, sur support microforme, papier, électronique et/ou autres formats.

L'auteur conserve la propriété du droit d'auteur et des droits moraux qui protège cette thèse. Ni la thèse ni des extraits substantiels de celle-ci ne doivent être imprimés ou autrement reproduits sans son autorisation.

In compliance with the Canadian Privacy Act some supporting forms may have been removed from this thesis.

While these forms may be included in the document page count, their removal does not represent any loss of content from the thesis.

Conformément à la loi canadienne sur la protection de la vie privée, quelques formulaires secondaires ont été enlevés de cette thèse.

Bien que ces formulaires aient inclus dans la pagination, il n'y aura aucun contenu manquant.

Canada

© Mehran Talebinejad, Ottawa, Canada, 2006

Abstract

In this thesis, we study fractal behavior of myoelectric signals (MESs). Mathematics and definitions behind fractal behavior is presented. Different methods of estimating the fractal dimension are discussed, including time domain-based methods (i.e. Katz method, Box-Counting method) and spectrum based methods (i.e. Power Spectrum Slope Method (PSSM) and General Power Spectrum Method (GPSM)). The GPSM is introduced in context of MESs for the first time. Using simulated MESs effects of its parameters (i.e. number of active motor units (MUs), firing rate and depth of active MUs) on estimated fractal dimension (eFD) and estimated fractal indicators (eFI) are analyzed. Spectrum based methods demonstrate characteristics that suggest superiority in discerning force effects (i.e. number of active MUs and firing rate) and geometric effects (i.e. depth of active MUs). Fractal behavior of MESs during Isometric Constant Force Contractions (ICFC) at different force and joint angles are analyzed. Results of the spectrum based methods suggest that they could possibly be used to estimate the joint angle independent of force. Fractal behavior of MESs during Isometric Voluntary Contractions (IVC) at different force and joint angles are analyzed as well. Results, although highly variable, remain consistent with the simulated results.

Acknowledgments

I wish to express sincere appreciation to each of my supervisors: Dr. Adrian Chan and Dr. Ali Miri for their assistance and guidance throughout this work.

In addition, special thanks are due to Dr. Richard Dansereau for his valuable suggestions.

I would like to thank my entire family for their support.

Above all, I dedicate this thesis to my father.

Table of Contents

List of Tables

List of Figures

List of Symbols

α	scaling exponent
α_{right}	estimated right hand slope using PSSM
α_{left}	estimated left hand slope using PSSM
λ	scaling factor
$\bar{a}$	average step size
$\dim_B F$	Box-Counting dimension of F
c	estimated scaling factor using GPSM
g	estimated lower frequency parameter using GPSM
$k_{\max}$	frequency in which maximum magnitude of power spectrum happens
q	estimated upper frequency parameter using GPSM
$n(x)$	white Gaussian noise
D	similarity dimension
$N_\delta(F)$	number of non-empty boxes to cover F
$N(k)$	complex spectrum of white Gaussian noise
$P(k_i)$	digitized power spectrum
$\hat{P}(k_i)$	approximated power spectrum
$\Pr\{\}$	probability density function

List of Abbreviations

eFD	estimated fractal dimension
eFI	estimated fractal indicator
ms	milliseconds
ANOVA	analysis of variance
BM	Brownian motion
FBM	fractional Brownian motion
FD	fractal dimension
FI	fractal indicator
FN	fractal noise
GPSM	general power spectrum method
ICFC	isometric constant force contraction
IFS	iterated function system
IVC	isometric voluntary contraction
MDF	median frequency
MES	myoelectric signals
MNF	mean frequency
MU	motor unit
MUAP	motor unit action potential
PSD	power spectrum density
PSDF	power spectrum density function
PSM	power spectrum method
PSSM	power spectrum slope method

RMS	root mean square
RSF	random scaling fractal
SFAP	single fiber action potential
SSFAP	surface single fiber action potential
SMUAP	surface motor unit action potential
WGN	white Gaussian noise

Chapter 1

Introduction

1.1 Introduction

Generally speaking, myoelectric signals (MESs) are the sum of electrical activity associated with a number of motor units (MUs), which are basic components of a muscle and its nerve supply. MESs are significantly influenced by measurement conditions but they still contain valuable information about recruitment and firing rate strategies of MUs. MESs are being widely used for better understanding of how muscles function. The forward problem is determining how specific mechanisms and phenomena influence MESs and the inverse problem is determining how these signals reflect these mechanisms and phenomena.

There has been much research done on relationships of MES features with force. For example, it is well established that amplitude of MES is well correlated with the produced force (i.e. increasing force will cause an increase in the amplitude) [1]. In the last decade there has been some effort in applying techniques that have been used for analyzing nonlinear dynamical systems and more specific chaotic dynamical systems for a better understanding of MESs [2-6].

Anmuth *et al.* [2] reported a linear correlation between muscle activation and estimated fractal dimension (eFD) of MES, which is a popular feature of a chaotic behavior related to fractional dimension of the strange attractors in the trajectories of the chaotic behavior. In this study, they collected surface MES from the first dorsal interosseous muscle at different levels of maximum voluntary contractions during isometric contractions and estimated the fractal dimension using the Katz method [7]. Gupta *et al.* [4] studied fractal dimension of surface MES using Katz method for estimating the fractal dimension during isokinetic contractions and also reported an increase in the eFD as the force is increased. Gitter *et al.* [3] also showed that eFD of MES from isometric contractions of the biceps, detected by a mono-polar needle electrode, is highly correlated with force. The eFD ranged between 1.1 to 1.4, increasing as force is increased; however, they used the Box-Counting algorithm [9, 10] for estimating the fractal dimension, which inherently saturates for fractal dimensions higher than 1.5 for time functions and is completely biased by amplitude (chapter 2) [9, 10]. Xiao *et al.* [8] tried to quantify the effects of recruitment number and firing rate of MUs on eFD using data simulated using the volume conductor model and demonstrated that eFD using Box-Counting method increases as recruitment number is increased and/or as firing rate is increased. Their work also suffers from the saturation of eFD using Box-Counting method [9, 10].

These results of increasing eFD with increasing force are not surprising because both the Box-Counting and Katz methods for estimating fractal dimension are computing the eFD from the time domain representation of the signal and are heavily influenced by the amplitude of the MES, which increases as the force production increases (chapter 4); therefore, the eFD, which is supposed to be related to the complexity of the signal, becomes a measure highly correlated with the signal amplitude, where even constant amplitude scaling would increase the eFD. Information delivered by this measure is not purely reflecting complexity of the signal and there is confusion about how much it is related to complexity and/or amplitude. In this thesis, two superior methods of quantifying the signal complexity are presented: Power Spectrum Method (PSM) and General Power Spectrum Method (GPSM).

Although effects of muscle force on amplitude and eFD of MESs have been examined and investigated [2-6], effects of joint angle on MESs features are still poorly understood and have remained unexamined in previous works. This work seeks to investigate and explain the relationships of joint angle and MES features, and more specifically, the relationship of joint angle and fractal properties of MESs. This includes an examination through MES simulations and actual MES measurements, with varying force levels and joint angles.

During isometric contractions, at different joint angles, the muscle length and other geometrical aspects of MUs are different. Effects of tissue filtering and electrode placement will significantly impose changes to both the time domain and frequency domain shape of the detected surface MES too. It is also of interest to find a method for estimating joint angle independent of force because changes in muscle length causes changes in the ability of the muscle to produce force. Conventional methods, such as amplitude estimation, are not able to deliver information that would be able to differentiate joint angle and force level combinations.

1.2 Thesis Organization

The rest of this thesis is organized as follows. Chapter 2 starts with the basic definitions and mathematics related to fractal geometry. In chapter 2, the Katz and Box-Counting methods of estimating fractal dimension are explained; these are currently the most commonly used methods for estimating fractal dimension of MESs reported in the literature. Limitations of these techniques are also discussed in chapter 2. Two new methods for estimating fractal dimension of a time series, using the power spectrum of the signal, are introduced: the Power Spectrum Method (PSM) and General Power

Spectrum Method (GPSM). These new methods will be compared and contrasted with the Katz and Box-Counting methods. A discussion on how these methods can be used for extraction of textural information as a fractal indicator, from power spectrum of the MESs, is provided in chapter 3. Chapter 4 discusses how number of recruitment, firing rate and depth of active motor units (MU) affect eFD of the MESs using Katz and Box-Counting methods, and the relationships of these MES variables with estimated fractal indicator (eFI) computed by the Power Spectrum Slope Method (PSSM) and GPSM. Simulated MES is used in this chapter to demonstrate these relationships. In chapter 5, effects of joint angle during Isometric Constant Force Contractions (ICFC) on the eFD and eFI are analyzed. Chapter 6 explains eFD and eFI in different joint angles during Isometric Voluntary Contractions (IVC). Chapter 7 provides a summary of the results and contributions, as well as proposing some future directions in this research area.

References

[1] R. Merletti, P.A. Parker, *Electromyography*. New Jersey: IEEE Press, 2004.

[2] C.J. Anmuth, G. Goldberg, N.H. Mayer, "Fractal dimension of EMG signals recorded with surface electrodes during isometric contractions is linearly correlated with muscle activation," *Muscle Nerve*, vol. 17, pp. 953-954, 1994.

[3] J.A. Gitter, M.J. Czerniecki, "Fractal analysis of the electromyographic interference pattern," *J. Neurosci. Meth.*, vol. 58, pp. 103-108, 1995.

[4] V. Gupta, S. Suryanarayanan, N.P. Reddy, "Fractal analysis of surface EMG signals from the biceps," *Int. J. Med. Inform.*, vol. 45, pp. 185-192, 1997.

[5] S. Chang, S.J. Hu, W.C. Lin, "Fractal dynamics and synchronization of rhythms in urodynamics of female Wistarrats," *J. Neurosci. Meth.*, vol. 139, pp. 271-279, Oct 2004.

[6] P. Ravier, O. Buttelli, R. Jennane, P. Couratier, "An EMG fractal indicator having different sensitivities to changes in force and muscle fatigue during voluntary static muscle contractions," *J. Electromyography Kinesiol.*, vol. 15, pp. 210-221, 2005.

[7] M.J. Katz, "Fractals and the analysis of waveforms," *Comp. Biol. Med.*, vol. 18, pp. 145-156, 1988.

[8] Z. Xu, S. Xiao, "Fractal dimension of surface EMG and its determinants," Engineering in Medicine and Biology society, *IEEE Proc.*, vol. 4, 1997, pp. 1570-1573.

[9] M. Al-Akaidi, *Fractal Speech Processing*. Cambridge: Cambridge University Press, 2004.

[10] M.J. Turner, J.M. Blackledge, P.R. Andrews, *Fractal geometry in digital imaging*. London: Academic Press, 1998.

Chapter 2

Fractals

Chaotic systems exhibit unpredictable behavior that do not appear to follow any order when analyzed with conventional methods; that is, looking at the output simply as a function of time or frequency. Instead, behavior of a chaotic system exhibits a geometrical feature, known as fractal structure. Fractal geometry is based on self similarity and fractal structures are self similar; that is, they look similar in different scales. The first part of this chapter presents an introduction on fractal profiles and how they are different in order of lacunarity and textural information along with descriptions of self similar and self affine fractal sets. The second part of this chapter presents the Weierstrass process, Fractional Brownian Motion (FBM) and Fractal Noise (FN) as examples of deterministic and stochastic fractal processes with known theoretical fractal dimensions. Finally, the Katz method, Box-Counting method, Power Spectrum Slope Method (PSM), and General Power Spectrum Method (GPSM) for computing the estimated fractal dimension (eFD) and estimated fractal indicator (eFI) are introduced. These methods are discussed and compared using the fractal processes mentioned previously in the third part of this chapter.

2.1.1 Fractal Profiles and Textural Information

Fractal or similarity dimensions are a measure of space filling, lacunarity, and complexity of the fractal profile. These qualities are known as textural information, which are not well defined by Euclidean geometry. According to Mandelbrot [1], "Texture is an elusive notion which mathematicians and scientists tend to avoid because they can not grasp it.

Engineers and artists can not avoid it, but mostly fail to handle it" and "In fact much of fractal geometry could pass as an implicit study of texture".

While there is no universally accepted mathematical definition for texture, Tamura *et al.* [2] defined six mathematical measures necessary for classifying a texture:

1. Coarseness (coarse versus fine). It is the most fundamental measure of a texture. A simple procedure for measuring coarseness in an image was presented by Rosenfeld [3], where this procedure detects largest size at which repetitive patterns are present.
2. Contrast (high versus low). Defined as sharpness of edges and period of repeating pattern.
3. Directionality (directional versus non-directional). This is average property over a given range.
4. Line-likeness (line-like versus blob-like). This is a supplementary aspect for other major ones like coarseness. A definition of line-likeness considers how probably the direction, at a specific point, is similar to one at a certain distance away.
5. Regularity (regular versus irregular). A fine texture is considered as a regular texture too. This aspect is close to coarseness and is related to how much coarseness, directionality and line-likeness change in the structure and is related to standard deviation of these features.
6. Roughness (rough versus smooth). It is another quality feature in an image close to coarseness.

Tamura *et al.* [2] defined mathematical definitions for all these measures and investigated the correlation between these measures and human perception.

Fractal geometry can provide textural information about a fractal profile in an alternative approach; that is, through geometrical, self similarity and self affinity aspects of the fractal profile. Concepts of self similarity and self affinity are presented in sections 2.1.2 and 2.1.3.

2.1.2 Self Similar Fractals

According to Mandelbrot [1], who coined the term fractal, "a fractal is by definition a set for which the Hausdorff dimension strictly exceeds the topological dimension, and a fractal is a shape made up of parts similar to the whole in some way".

In other words, a strictly self similar set is the union of smaller similar copies of itself. Considering a bounded set A in a Euclidean space, then the set A is said to be self similar if A is the union of N distinct (non-overlapping) copies of itself, each of which has been scaled by a ratio $r < 1$ in all coordinates. A strictly self similar fractal profile can be defined by the relationship,

$$Nr^D = 1 \text{ or } D = -\frac{\ln N}{\ln r} \qquad 2.1$$

Such a self similar set has a Hausdorff and box dimension of D [3]. More general fractal sets are composed of the union of N distinct subsets each of which is scaled down by a ratio r_i, $1 \le i \le N$, from the original in all coordinates. The fractal dimension of such fractal profile is given by a generalization of Eqn 2.1, namely,

$$\sum_{i=1}^{N} r_i^D = 1 \qquad 2.2$$

D is also known as similarity dimension.

For stochastic processes, deterministic features of the fractal may change in different scales but statistical properties at all scales are the same; therefore, these fractals are statistically self similar (statistical scale invariance).

2.1.3 Self Affine Fractals

Self similar sets are made up of subsets scaled in all coordinates. In a more general case, scaling can be done in different coordinates [3]. For example consider a curve $f(x)$ that satisfies,

$$f(\lambda x) = \lambda^{\alpha} f(x) \rightarrow \forall \lambda > 0 \qquad 2.3$$

where λ is the scaling factor and α is the scaling exponent. This equation implies that a scaling of the x coordinate by λ gives a scaling of the f coordinate by a factor λ^{α}; this is an example of self affinity. The Hausdorff and Box-Counting dimensions of this curve are related to the scaling exponent through a linear transformation and this exponent serves as a fractal indicator (FI) [3].

In this case, if a stochastic process performs statistical self affinity it is called a Random Scaling Fractal (RSF). An RSF signal $f(x)$ has the following characteristic property,

$$\Pr\{f_{\lambda}(x)\} = \lambda^{-\alpha} \Pr\{f(\lambda x)\} \qquad 2.4$$

where $\Pr\{.\}$ denotes the probability density function.

2.2 Deterministic and Stochastic Fractal Processes

Deterministic fractals are usually generated through some Iterated Function System (IFS) and stochastic fractals are used to model a variety of natural profiles. Stochastic fractals can also be considered to be the solutions of certain classes of stochastic differential equations of fractional order. Generating fractal profiles with known theoretical fractal dimension is of interest because they provide a platform for analyzing features of a fractal profile with different fractal dimensions and a measure of effectiveness for fractal dimension estimation methods. Deterministic Weierstrass process, Fractional Brownian Motion (FBM), and Fractal Noise (FN) are three popular examples of synthetic fractal profiles with known theoretical fractal dimension and they will be introduced in the following subsections.

2.2.1 Weierstrass Process

Weierstrass process is an example of a self affine fractal. This fractal structure like most of the deterministic fractals is generated through an IFS given by Eqn 2.5,

$$f(x)=\sum_{i=1}^{\infty}\lambda^{-Si}\cos(\lambda^{i}x),\ \lambda>1,\ 0<S<1 \qquad 2.5$$

This function has the scaling property that satisfies Eqn 2.6 [4],

$$f(\lambda x)=\lambda^{2-S}f(x),\forall x\in R \qquad 2.6$$

which means the curve of this function (the trajectory) has a fractal dimension *D=2-S*, where scaling exponent is *2-S*. The curve becomes smooth with low values of *D*, and when *D* increases toward *2*, the curve tends to occupy *2D* Euclidean dimension and becomes rougher (Figure 2.1).

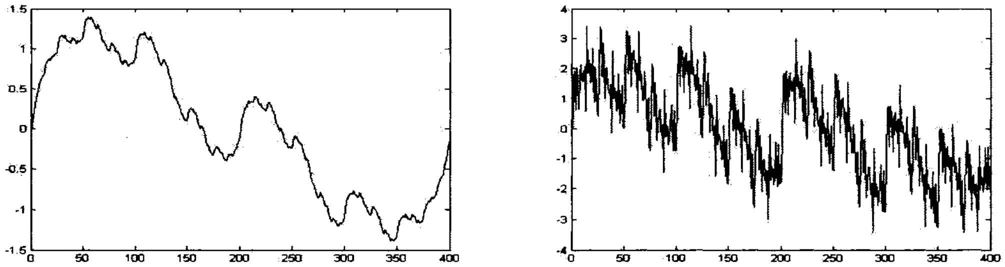

(a) FD=1.1 (b) FD=1.9

Figure 2.1: Trajectory of Weierstrass process with fractal dimensions (a) 1.1 and (b) 1.9. As the fractal dimension increases towards 2 the curve gets rougher and more space filling.

2.2.2 Fractional Brownian Motion

Brownian motion is a relatively common process in nature. Fractional Brownian Motion (FBM) is a stochastic fractal, based on an analogy to deterministic fractals. To generate a random fractal, again IFS can be used while scaling factors are random. Many natural phenomena can be best modeled with FBM. Generally speaking, FBM is a Gaussian process with a special covariance structure and incremental features. [3, 5]

FBM of index-α ($0 < \alpha < 1$) is defined to be a Gaussian process $X : [0,\infty) \rightarrow R$ on some probability space such that $X(t)$ is continuous and $X(0)=0$. For every $t \geq 0$ and $h > 0$ the increment $X(t+h)-X(t)$ has a normal distribution with mean zero and variance $h^{2\alpha}$, such that,

$$\Pr(X(t+h) - X(t) \leq x) = (2\pi)^{-1/2} h^{-\alpha} \int_{-\infty}^{x} \exp(-u^2/2h^{2\alpha}) du \qquad 2.7$$

Index-α FBM has fractal dimension of $D=1-\alpha$. FBM is a RSF which means it satisfies the scaling property of RSFs,

$$\Pr\{X(hx)\} = h^{2\alpha} \Pr\{X(x)\} \qquad 2.8$$

There are different methods for simulating the exact process [6, 7], such as Hosking method. The Hosking method (also known as the Durbin or Levinson method) is an algorithm to simulate a general stationary Gaussian process. Simulated FBM trajectories using Hosking method with FRACLAB toolbox [13] in Figure 2.2 show, as fractal dimension of FBM increases the trajectory becomes rougher and tends to occupy 2D Euclidean space.

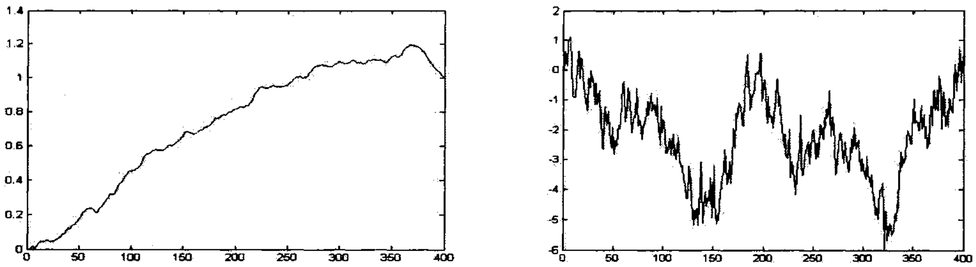

(a) FD=1.1 (b) FD=1.9

Figure 2.2: Trajectory of FBM process simulated using Hosking method with FRACLAB toolbox [13], with fractal dimensions (a) 1.1 and (b) 1.9. As the fractal dimension increases towards 2 the curve gets rougher and more space filling.

2.2.3 Fractal Noise

Consider a fractional order stochastic differential equation like Eqn 2.9,

$$\frac{d^q}{dx^q} f(x) = n(x) \qquad 2.9$$

It can be shown that when n is a White Gaussian Noise (WGN) with a constant power spectrum (assumed to be dimensionless), the solution to this equation is consistent with definition of a RSF (Appendix A) [8, 9] and is known as fractal noise; which means the curve of the $f(x)$ satisfies Eqn 2.10,

$$\Pr\{f_\lambda(x)\} = \lambda^{-q} \Pr\{f(\lambda x)\} \qquad 2.10$$

In other words with fractional integration of WGN or smoothing it with a fractional order fractal noise is obtained (Figure 2.4).

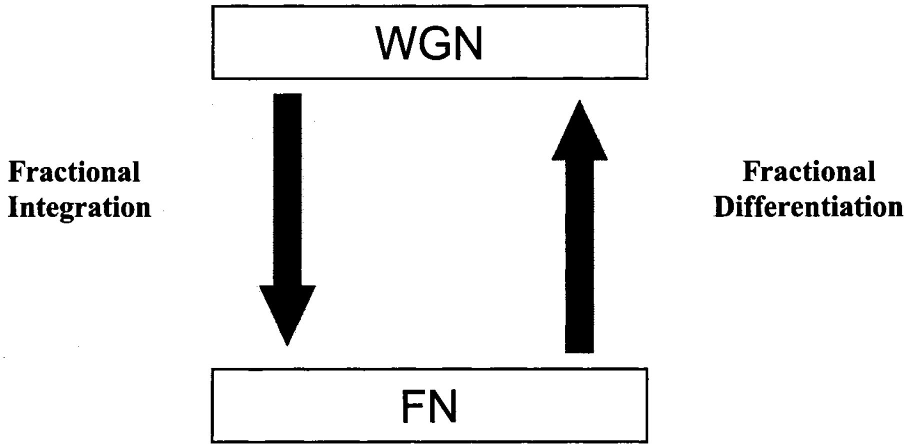

Figure 2.3: Relationship between WGN and FN. Differentiation is the roughing process and integration is the smoothing process.

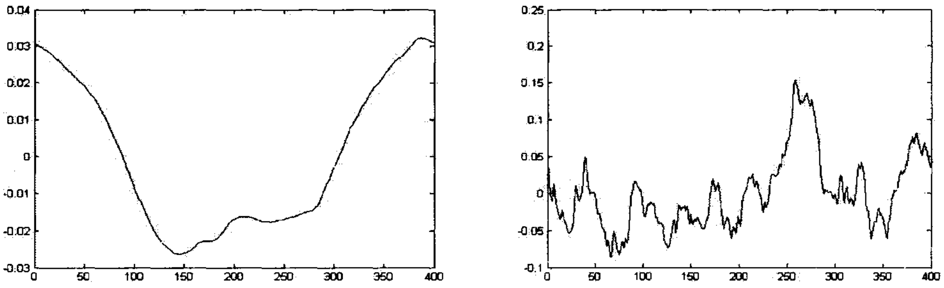

(a) FD=1.1 (b) FD=1.9

Figure 2.4: Fractal noise with fractal dimension (a) 1.1 and (b) 1.9. A fractal noise with low fractal dimension is well smoothed version of WGN (smoothed with a high order) while a fractal noise with higher dimension is rougher.

2.3 Estimating Fractal Dimension of One Dimensional Time Series

There are many ways for computing the eFD of a digital sequence. The eFD can be computed using the time domain representation of the signal (e.g. Box-Counting [8, 9], walking divider [8, 9] and Katz [10]), in the time-frequency domain (wavelet based methods [11]), or from the power spectrum representation of the digital sequence (Power Spectrum Slope Method (PSSM) [8, 9] and General Power Spectrum Method (GPSM) [8, 9]). In this section, two conventional methods for estimating fractal dimension of MESs are reviewed and discussed: the Katz and Box-Counting methods. PSM and GPSM methods for estimating fractal dimension are also introduced and compared to the two conventional approaches. The Weierstrass process, FBM, and FN are used as test signals to demonstrate and evaluate the various methods for computing the eFD.

2.3.1 Katz Method

Mandelbrot [1] showed that, length-area characteristics of a planar object are related to the fractal dimension of the object. Fractal dimension D of a planar waveform is generally related to total length of the curve L and the planar extent or diameter d through the power law [10, 12]; that is,

$$D = \frac{\log L}{\log d} \qquad 2.10$$

For a digital sequence, L can be easily computed as sum of Euclidean distances between successive points.

$$L = \sum_i \sqrt{(x(i+1) - x(i))^2 + (y(i+1) - y(i))^2} \qquad 2.11$$

where x and y are coordinates of each point in the sequence and for a digital sequence $x(i+1) - x(i)$ is always one and y corresponds to the amplitude of the signal at each point. In the Katz method [10]; the diameter d is approximated as the farthest distance between the starting point and any other point of the waveform.

$$d = \max(\sqrt{(x(i) - x(1))^2 + (y(i) - y(1))^2}), \ \forall i : 1 \le i \le N \qquad 2.12$$

where N is the number of samples in the waveform.

Using Eqn 2.12 directly will cause confusion about measurement units. If the length and diameter of the curve were calculated in different units, the corresponding eFDs would be different. This problem is due to the fact that this method is working in a discrete space rather than in a continuum. One practical way is to work in a standard space with defining a standard unit size as the smallest wiggle of interest where in case of a digital signal it can be the average size $\bar{a}$ between successive points then Eqn 2.9 can be rewritten as,

$$D = \frac{\log L/\bar{a}}{\log d/\bar{a}} \qquad 2.13$$

Defining *n* as number of points in the sequence, Eqn 2.13 can be rewritten as,

$$D = \frac{\log(N)}{\log(N) + \log(d/L)} \qquad 2.14$$

where $N = \frac{L}{\bar{a}}$.

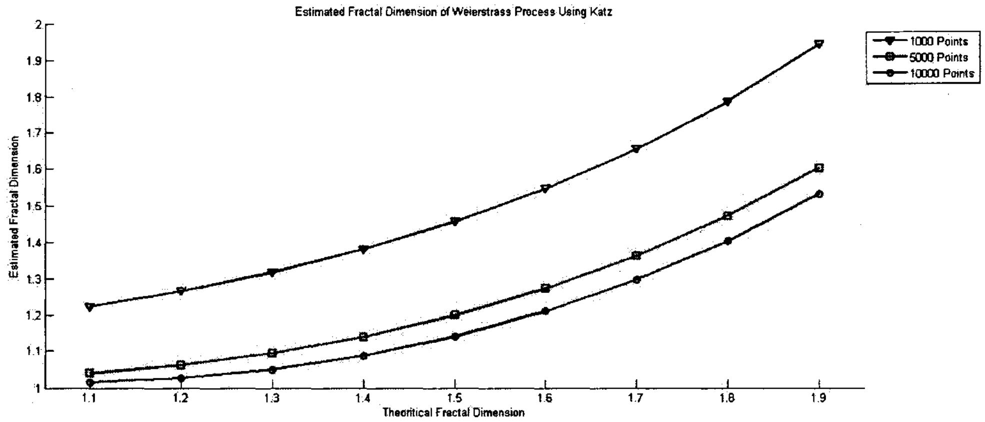

(a)

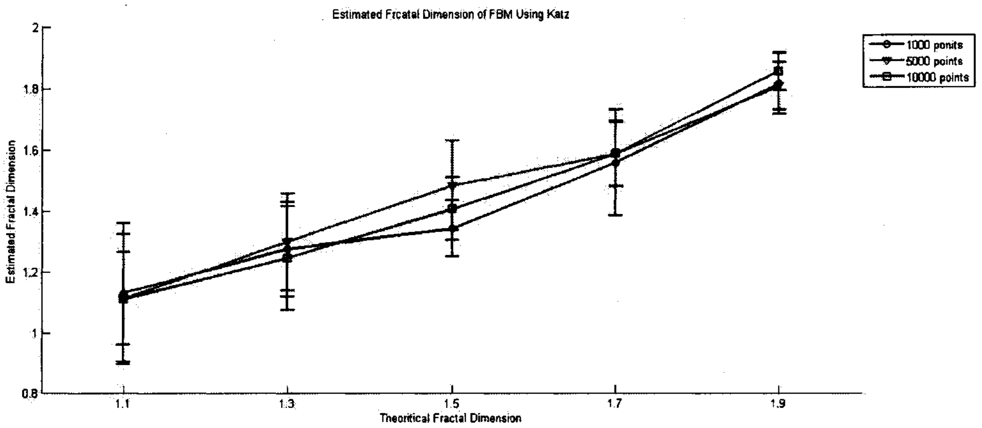

(b)

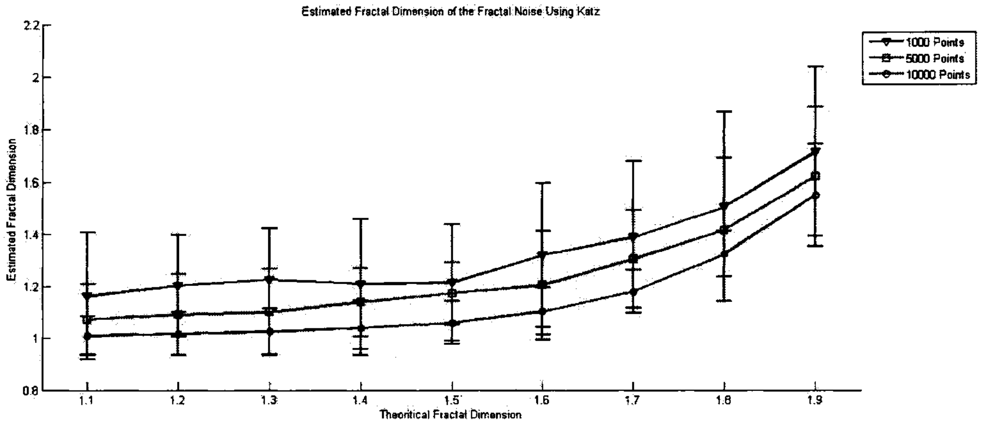

(c)

Figure 2.5: Estimated fractal dimension using Katz method of (a) Weierstrass process, (b) FBM, and (c) FN versus theoretically known fractal dimensions. Results for FBM and FN are the average and standard deviation obtained from ten iterations.

This Katz method is simple and fast. Figure 2.5 shows eFD of the Weierstrass process, FBM, and FN versus theoretical fractal dimensions. For the FBM and FN, the eFD was computed for 10 different test signals to generate the mean and variance values. As the number of the points in the digital signal increases, the eFD is decreased because length and diameter of the curve are not comparable to the number of the points anymore. In addition, the amplitude of the signal affects the eFD of the signal too.

By definition, dimension of an object should not change by amplifying it in all coordinates; however, the Katz method is computing the eFD directly from the time-space representation of the signal, so amplifying the signal will change the area the curve of the signal is occupying and hence the eFD. Moreover, fractal dimension of a planar waveform in a space-space representation is related to the length and diameter of the waveform through Eqn 2.10 and for sampled time functions (i.e. space-time representation) the Euclidean distance $x(i+1)-x(i)$, which corresponds to time, is always one. This makes Katz method unsuitable in the case of time functions.

2.3.2 Box-Counting Method

The Box-Counting method [8, 9] is a popular method based on the Box-Counting definition of fractal dimension. This method can be used for estimating fractal dimension of fractal dust (0<eFD<1), waveforms (1<eFD<2), images (2<eFD<3), and volumes (3<eFD<4). Box-Counting dimension states, if F is a bounded set of $\Re^n$, and $N_\delta(F)$ be the smallest number of sets of diameter at most δ which can cover F, Box-Counting dimension of F is defined as [3],

$$\dim_B F = \lim_{\delta \to 0} \frac{\log N_\delta(F)}{-\log \delta} \qquad 2.15$$

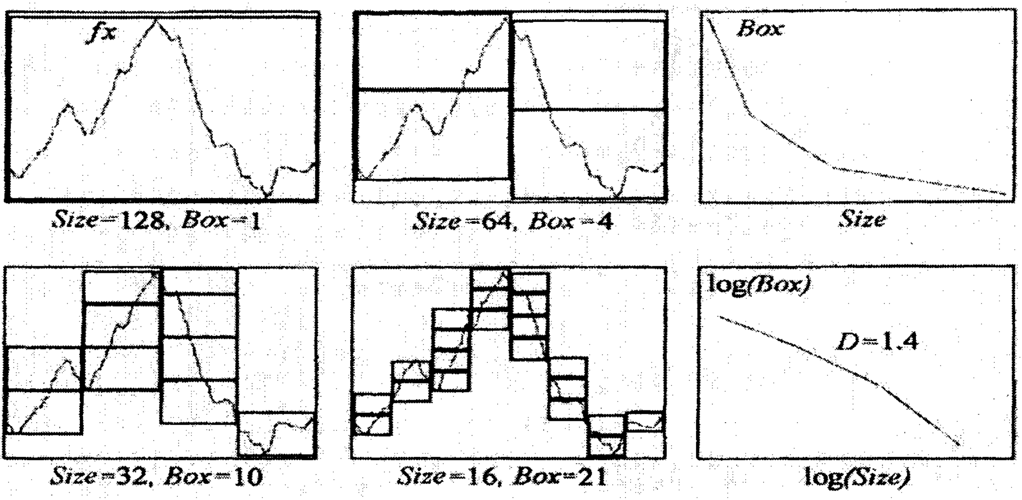

Figure 2.6: Showing four iterations of Box-Counting method, estimated fractal dimension is the slope of the least squares fit, reproduced from [8].

In general, to estimate the fractal dimension using Box-Counting method, the fractal is covered by a grid of boxes with side length δ and number of non-empty boxes $N_{\delta}(F)$ is counted, and recursively different sized boxes are used. The slope obtained in a bi-logarithmic plot of the number of boxes against their side length gives the eFD (i.e. bi-logarithmic derivative) (figure 2.6) [8, 9].

This method gives accurate results for dimensions up to 0.5 above the topological dimension (i.e. 0 to 0.5 for fractal dust, 1 to 1.5 for waveforms, 2 to 2.5 for images and 3 to 3.5 for volumes, etc.). For fractals with higher dimension it gets saturated approximately 0.6 above the topological dimension [8, 9]. These conditions are even worse in the case of stochastic processes and underestimation happens in most cases. Figure 2.7 shows eFD of Weierstrass process, FBM and FN using Box-Counting method (FRACLAB toolbox [13]) versus theoretically known fractal dimensions. To estimate the fractal dimension using Box-Counting method the curve of the signals was covered by square boxes with side length of size $\frac{1}{2^n}$. The n indicates the recursion's number which was an integer between 1 and 8 for this study. Another drawback of Box-Counting method, as results show, is how accuracy of estimation depends on the number of points in a digital sequence.

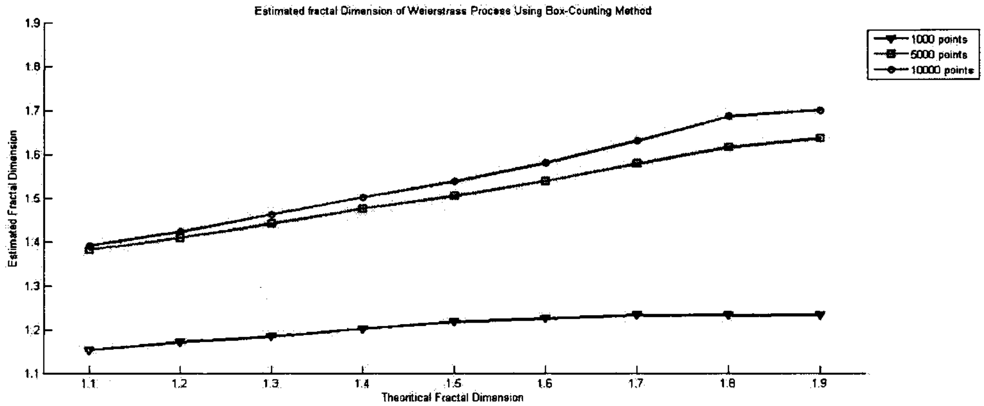

(a)

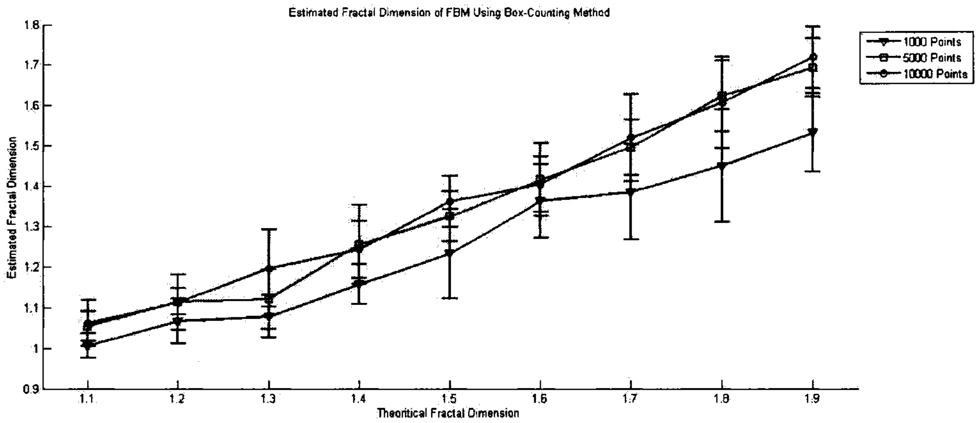

(b)

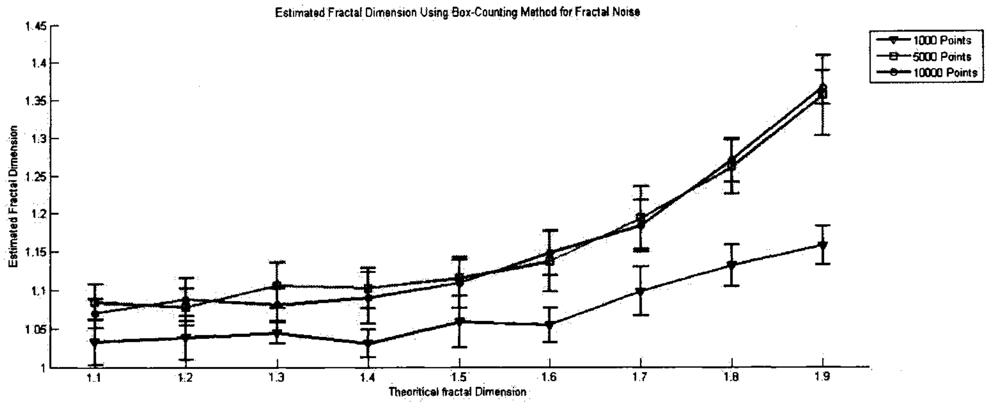

(c)

Figure 2.7: Estimated fractal dimension using the Box-Counting method of (a) Weierstrass process, (b) FBM and (c) FN versus theoretically known fractal dimensions. Results for FBM and FN are the average and standard deviation obtained from ten iterations.

This method gives poor estimations for signals with less samples and underestimation happens in most cases. The variance of estimation decreases as number of the points is increased too.

2.3.3 Power Spectrum Method

Power spectrum method (PSM) [8, 9] is based on the fact that fractal profiles show a $1/k^{\alpha}$ behavior in the power spectrum; that is, the power or magnitude of the spectrum shows a linear variation between logarithm of the magnitude and logarithm of the frequency *k*. The slope of the line which can approximate this relationship is related to the fractal dimension of the fractal profile through a linear transformation and serves as a fractal indicator (FI) [12].

Consider a fractional order stochastic differential equation like Eqn 2.16,

$$\frac{d^q}{dx^q} f(x) = n(x) \qquad 2.16$$

The solution to this equation is consistent with the definition of a RSF (appendix A); that is,

$$\Pr\{f_\lambda(x)\} = \lambda^{-q}\Pr\{f(\lambda x)\} \qquad 2.17$$

Consider estimated power spectrum of the digitized RSF,

$$P(k_i): i = 1,2,3,\dots,N \qquad 2.18$$

$1/_{k^\alpha}$ behavior means these data can be approximated by $\hat{P}(k_i) = \frac{c}{|k_i|^{2q}} = \frac{c}{|k_i|^{\beta}}$. Defining the error as,

$$e(\beta,C) = \sum_i [\ln P(k) - \ln \hat{P}(k_i)]^2 = \sum_i [\ln P(k_i) - (C - \beta \ln|k_i|)]^2 \qquad 2.19$$

where C=ln c, using least squares β can be obtained as,

$$\frac{\partial e}{\partial \beta} = 0 \Rightarrow \beta = \frac{N\sum_i (\ln P(k_i))(\ln|k_i|) - \left(\sum_i \ln|k_i|\right)\left(\sum_i \ln P(k_i)\right)}{\left(\sum_i \ln|k_i|\right)^2 - N\sum_i (\ln|k_i|)^2} \qquad 2.20$$

Using this method, the spectral exponent β can be estimated directly [8, 9]. β is related to the fractal dimension through a linear transformation and can be considered as a FI. Figure 2.8 shows transformed eFI (i.e. eFD) of Weierstrass process, FBM, and FN versus theoretically known fractal dimensions using the PSM. The Yule-Walker method, with a 6th order autoregressive model, was used for estimating the power spectrum. PSM is one of the most direct and powerful methods for analysis of fractal behavior. One significant feature of this method is that the eFI of a digital signal remains the same even if it is amplified or attenuated. Although $1/_{k^\alpha}$ behavior in power spectrum is a property of many signals that are found in nature, it is not appropriate to all types of signals and/or to the whole spectrum shape. Many signals do have a high frequency decay for which the fractal model is appropriate but the complete power spectrum may have characteristics for which a simple $1/k^{\alpha}$ power law is not appropriate. This had led to the development of spectral partitioning algorithms which attempt to extract the most appropriate part of the spectrum for which the $1/k^{\alpha}$ power law applies [8, 9].

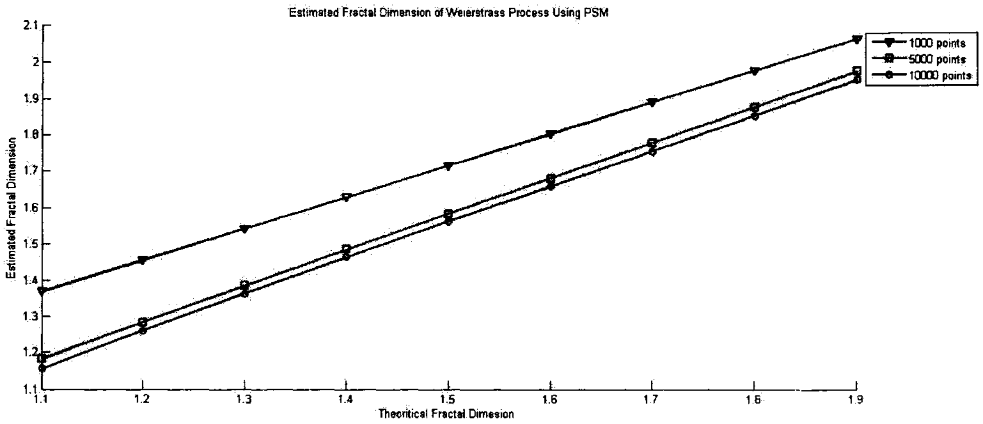

(a)

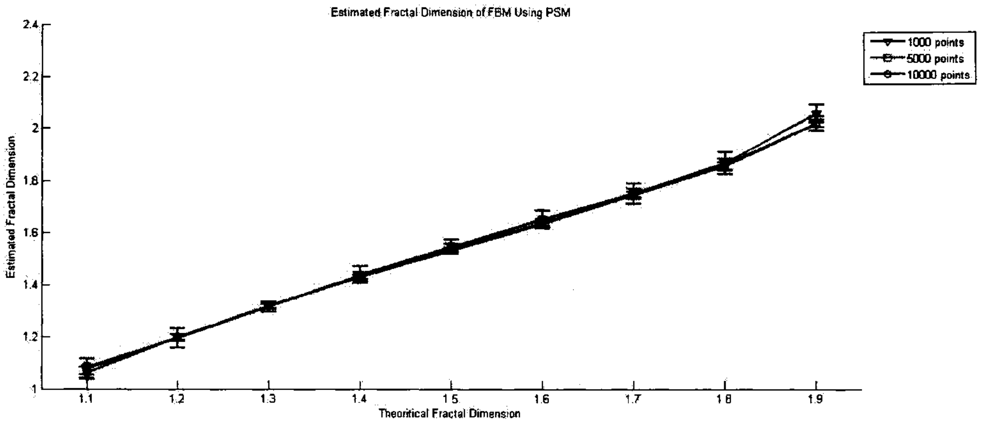

(b)

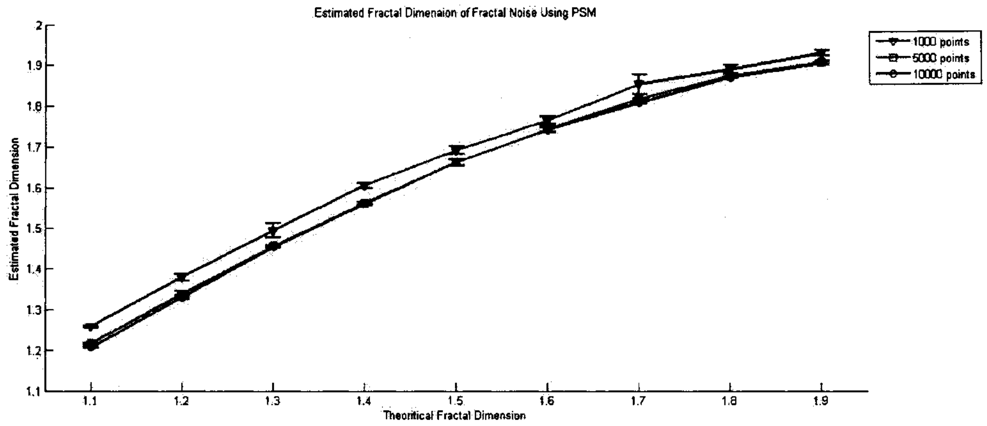

(c)

Figure 2.8: Estimated fractal dimension using the PSM of (a) Weierstrass process, (b) FBM and (c) FN versus theoretically known fractal dimensions. Results for FBM and FN are the average and standard deviation obtained from ten iterations.

2.3.4 General Power Spectrum Method (GPSM)

In this method, a more general model has been proposed where the power spectrum of a stochastic signal is assumed to be in the form of Eqn 2.20 [8, 9],

$$P(k) = \frac{c|k|^{2g}}{(k_0^2 + k^2)^q} \qquad 2.21$$

Clearly this model reduces to $P(k) = \frac{c}{|k|^{2q}}$, the model of $1/k^{\alpha}$ behavior, if $g = 0$, $k_0 = 0$ and $1 < q < 2$, which is the same as the PSM. For nonzero values, the fractal dimension of the signal with such a power spectrum is related to g and q through a linear transformation because a profile with such a power spectrum is self affine and consistent with Eqn 2.22 (Appendix B); that is,

$$\Pr[f'(x,k_0)] = \lambda^{g-q} \Pr[f(\lambda x, k_0/\lambda)] \qquad 2.22$$

This model encompasses the fractal model and other stochastic processes such as the Ornstein-Uhlenbeck and Bermann processes [8, 9]. Both parameters g and q contain textural information and they can be used for textural segmentation of a wide range of signals and images. In case of using this model to characterize texture, a combination of parameters g and q (their product for example) is taken to be a measure of texture.

The general four parameter problem (unknown c, g, k_0 and q), is not easily solved for digital sequences; however having a good estimate for k_0, using standard least squares method c, g, and q can be computed for a signal. Consider defining the error as,

$$e(g,q,C)=\sum_i\left[(\ln P(k_i)-\ln \hat{P}(k_i)^2\right] \qquad 2.23$$

where C=ln c, $P_i = P(k_i) : i = 1,2,3,...,N$ is the discrete power spectrum of the signal and

$\hat{P}(k_i)=\dfrac{c|k_i|^{2g}}{(k_0^{\ 2}+k_i^{\ 2})^q}$ is its expected form. The error can be rewritten as Eqn 2.24,

$$e(g,q,C)=\sum_i\left[\ln P_i-2g\ln|k_i|-C+q\ln\left(k_0^{\ 2}+k_i^{\ 2}\right)\right]^2 \qquad 2.24$$

error is minimum when, $\dfrac{\partial e}{\partial g}=0$, $\dfrac{\partial e}{\partial q}=0$, $\dfrac{\partial e}{\partial C}=0$.

Differentiating the error, the parameter set (g, q, C) can be obtained from the solution of the following linear system equation,

$$\begin{bmatrix} a_{11} & a_{12} & a_{13} \\ a_{21} & a_{22} & a_{23} \\ a_{31} & a_{32} & a_{33} \end{bmatrix}\begin{bmatrix} g \\ q \\ C \end{bmatrix}=\begin{bmatrix} b_1 \\ b_2 \\ b_3 \end{bmatrix} \qquad 2.25$$

where

$$a_{11} = \sum -2\left(\ln|k_i|\right)^2$$
$$a_{12} = \sum \ln(k_0^2 + k_i^2)\ln|k_i|$$
$$a_{13} = \sum -\ln|k_i|$$
$$a_{21} = \sum 2\ln|k_i|\ln(k_0^2 + k_i^2)$$
$$a_{22} = \sum -\left(\ln(k_0^2 + k_i^2)\right)^2$$
$$a_{23} = \sum \ln(k_0^2 + k_i^2)$$
$$a_{31} = \sum -2\ln|k_i|$$
$$a_{32} = \sum \ln(k_0^2 + k_i^2)$$
$$a_{33} = \sum -1 = -N$$
$$b_1 = -\sum \ln P_i \ln|k_i|$$
$$b_2 = \sum \ln P_i \ln(k_0^2 + k_i^2)$$
$$b_3 = -\sum \ln P_i$$

Assuming we have actual values of g, k_0 and q, Eqn 2.21 has a maximum when,

$$\frac{d}{dk}\ln P(k) = \frac{2g}{k} - \frac{2kq}{k_0^2 + k^2} = 0 \qquad 2.26$$

this implies maximum value of *P(k)* occurs at frequency k_{max} given by,

$$k_{max} = k_0\sqrt{\frac{g}{q-g}}, \; q > g \qquad 2.27$$

Initial estimate of k_0 can be obtained from Eqn 2.28,

$$k_0 = k_{max}\sqrt{\frac{q-g}{g}}, \; q > g \qquad 2.28$$

where k_{max} is the frequency corresponding to the maximum value of the power spectrum. Having obtained k_{max}, with the first approximation $k_0 = k_{max}$, k_0 can be adapted through an iteration procedure with different results of Eqn 2.25 and Eqn 2.28. For pure fractal profiles like FN or FBM with a log-log power spectrum like Figure 2.9, $g = 0$ and $k_0 = 0$

and GPSM will reduce to PSM; therefore, graphs of the eFI using the GPSM for the Weierstrass process, FBM, and FN processes are not shown.

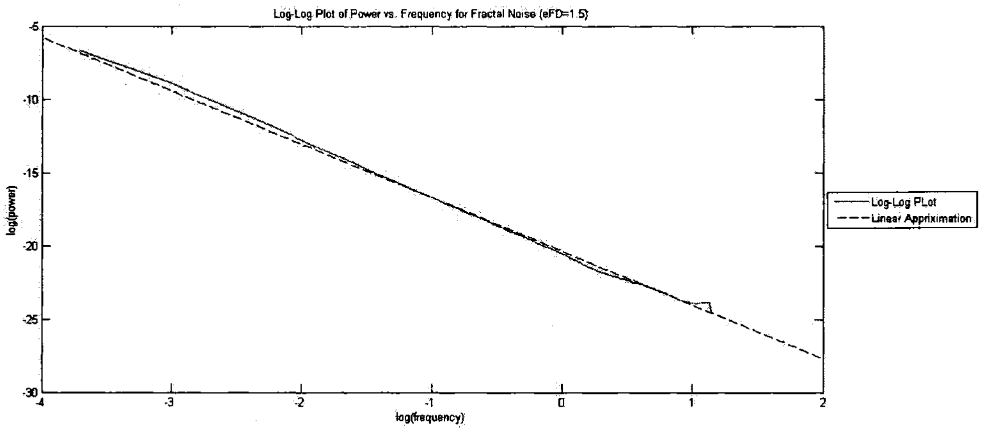

Figure 2.9: Approximating log-log power graph of the fractal noise with a line, slope of this line is related to fractal dimension through a linear transformation [12, 13].

2.3.5 Comparison

Table 2.1 compares variances of eFD and speed of estimation between Katz method, Box-Counting method and PSM. The time duration was determined by running the algorithms on a Pentium M 1.4 GHz computer with 512 MB RAM in Matlab version 7.0.4.

Table 2.1: Comparison between variance of eFD and speed of estimation.

	Mean variance of eFD of 1000 sample FBM	Mean variance of eFD of 1000 sample fractal noise	Mean variance of eFD of 10000 sample FBM	Mean variance of eFD of 10000 sample fractal noise	Time duration for estimating FD of 10000 sample fractal noise
Katz	0.65	0.72	0.63	0.75	11 sec
Box-Counting	0.53	0.59	0.23	0.31	45 sec
PSM	0.05	0.07	0.02	0.02	15 sec

The Katz method uses a very simple mathematical equation to compute the eFD and is faster than the two other methods; however, the variance of Katz method results are higher, which does not reduce as the number of points in the sequence is increased. Box-Counting method is computationally expensive and time consuming due to the recursive nature of the algorithm; moreover, in order to increase accuracy and reduce the variance of the results for Box-Counting method a large data set is needed. The computational time for the PSM is relatively short. The PSM used can be accurate without the need for a large number of samples. In addition, the variance of the PSM is approximately an order of magnitude better than the Katz method or Box-Counting method. In the case of these three test signals (i.e. Weierstrass process, FBM and FN) the PSM provides the most accurate results with the smallest variance.

References

[1] B. B. Mandelbrot, *Fractal Geometry of Nature*, Freeman-Oxford Press 1983.

[2] Hideyuki Tamura, Shunji Mori and Takashi Yamawaki, "Textural features corresponding to visual perception, IEEE Trans on Systems, Man and Cybernetics, vol. 6, 1978 pp. 460-473.

[3] Kenneth Falconer, *Fractal Geometry*, Wiley press, 2003.

[4] Kenneth Falconer, *Fractal Geometry of Fractal Sets*, Cambridge University press, 1986.

[5] Ning Lu and Wei-Kao Lu, *Fractal Imaging*, Elsevier, 1997.

[6] J.R.M. Hosking, "Modeling persistence in hydrological time series using fractional differencing", Water resources research, vol.20, 1984 pp. 1898-1908.

[7] Ton Dieke, "Simulation of fractional Brownian motion", Ph.D. dissertation, University of Twente, Department of Mathematical Sciences, Amsterdam, Netherlands, 2004.

[8] M. Al-Akaidi, *Fractal Speech Processing.* Cambridge: Cambridge University Press, 2004.

[9] M.J. Turner, J.M. Blackledge, P.R. Andrews, *Fractal geometry in digital imaging.* London: Academic Press, 1998.

[10] M.J. Katz, "Fractals and the analysis of waveforms," *Comp. Biol. Med.*, vol. 18, pp. 145-156, 1988.

[11] Cornelius T. Leondes, Medical Imaging Systems Techniques and Applications Brain and Skeletal Systems, Taylor francis (UK) Press, 1997.

[12] John C. Russ, Fractal Surfaces, Springer Press, 1994.

[13] FRACLAB, http://complex.inria.fr/index.php?page=fraclab

Chapter 3

Fractal Analysis of Myoelectric Signals

In chapter 2, the concept of fractals was introduced, along with methods of estimating the fractal dimension, a measure of a signal's texture or complexity. In this chapter, we review previously reported work on fractal analysis of MESs.

It is well established that amplitude of MES increases as the produced force increases [1]; however, there is an inconsistency about how force affects frequency content and spectral features of the MES. This chapter is divided into three parts: the first part contains a review on the relationship between amplitude and eFD; the second part contains a discussion on relationship of spectral features and eFD; and the third part is dedicated to GPSM and how this method is adopted for MESs.

3.1 Muscle Force, Myoelectric Signal Amplitude, and Fractal Dimension

Force production in a muscle is regulated by two main mechanisms [1]:

1. spatial recruitment: recruitment of additional MUs, which results in an increase in number of active MUs, and
2. temporal recruitment: increase of firing rate of the already active MUs.

These two mechanisms are present in different proportions in different muscles [2]. The amplitude of the surface MES depends on both the number of active MUs and their firing rate. Estimating muscle force from the amplitude of MES is attractive and has been addressed experimentally by many researchers [3-6]. In some muscles such those controlling the fingers, the relationship between force and amplitude of MES was found to be linear [4, 5]. This relationship was found to be closer to a parabolic shape in other muscles such as biceps [5, 6]. Overall it is well established that amplitude of MES increases as the produced force increases [1].

Anmuth *et al.* [7] reported a linear correlation between the eFD of MES and muscle activation level (figure 3.1). In this study, they collected surface MES from the first *dorsal interosseous* muscle at different levels of maximum voluntary contractions (MVC) during isometric contractions and determined the eFD using the Katz method [8]. This method is based on the fact that, length-area characteristics of a planar object are related to the fractal dimension of the object (section 2.3.1).

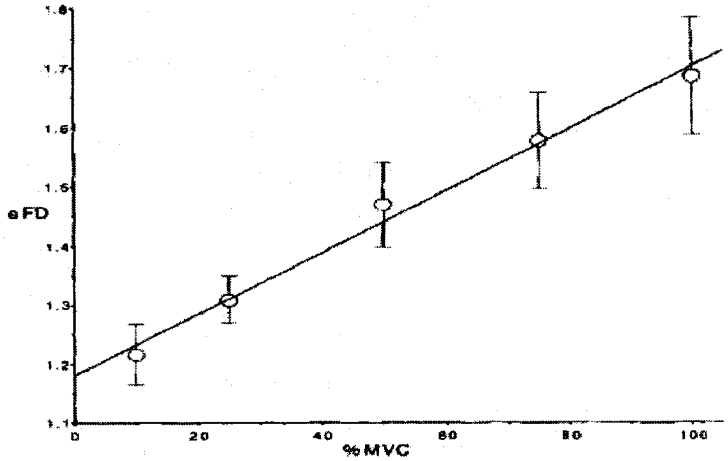

Figure 3.1: Linear correlation between eFD (Katz method) of MES and muscle activation level, reproduced from [7].

As previously discussed, an increase in force production results in an increase in MES amplitude. Simple amplitude scaling (i.e. multiplying the signal by a constant) will increase the length of the signal trajectory; meanwhile, the diameter of the signal curve is mainly dictated by the number of samples in the digital sequence (chapter 2.3.1). This limitation, which is imposed by discrete data, will cause the eFD of a digital signal using Katz method to increase if the signal is amplitude scaled by a constant value. High correlation between eFD of MES and different levels of muscle activation in Anmuth *et* *al.* [6] are likely due to this limitation of Katz method; that is, the eFD are providing an associated measure of MES amplitude rather than a measure of texture or signal complexity.

Gupta *et al.* [10] studied fractal dimension of surface MES collected from biceps during isokinetic contractions. In this study, they also used Katz method for computing the eFD and similarly reported an increase in eFD as the force is increased (figure 3.2).

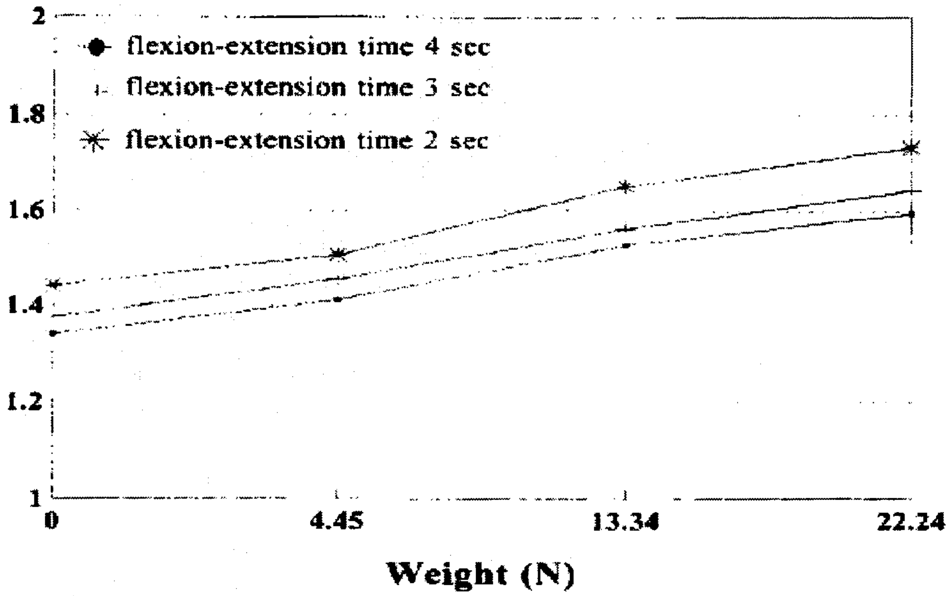

Figure 3.2: Increase in the fractal dimension as the force is increased, reproduced from [10].

Force was regulated by different weights in this experiment during different rates of flexion and extension of the arm. Handling higher weights by the muscle requires a higher number of active MUs and a higher firing rate in any muscle length or joint angle. Increasing the number of active MUs and firing rate implies an increase in the amplitude again and hence an increased eFD. Results of this study are also affected by limitations of the Katz method that were discussed, and increased eFD for increased weights is mainly the result of increased amplitude of MES.

Gitter *et al.* [9] also showed that fractal dimension of MES from the biceps, detected by a mono-polar needle electrode during isometric contraction, is highly correlated with force (figure 3.3). In this work, different levels of maximum voluntary contraction (MVC) were found to be correlated with eFD, as computed by the Box-Counting method. Their results are affected by the fact that Box-Counting method deals with the time domain representation of the signal (section 2.3.2). As the amplitude increases number of boxes used for covering the signal's curve increases and hence the eFD increases. Thus, the Box-Counting method, as with the Katz method, is strongly influenced by simple amplitude scaling.

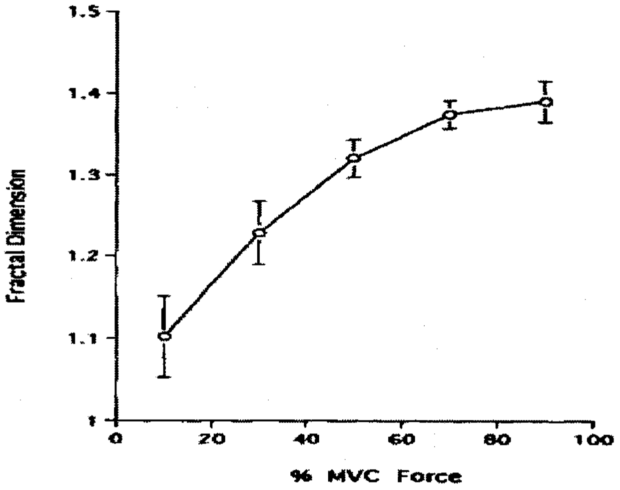

Figure 3.3: Higher levels of maximum voluntary contraction resulted in a higher eFD, reproduced from [9].

Xu *et al.* [11] tried to quantify the effects of recruitment number and firing rate of MUs on fractal dimension using data simulated using the volume conductor model. They demonstrated that eFD, computed using Box-Counting method, increases as recruitment number is increased and/or as firing rate is increased. Their results are in the same line with three previous studies, with an increase in amplitude of simulated MES being correlated with an increased eFD (figure 3.4).

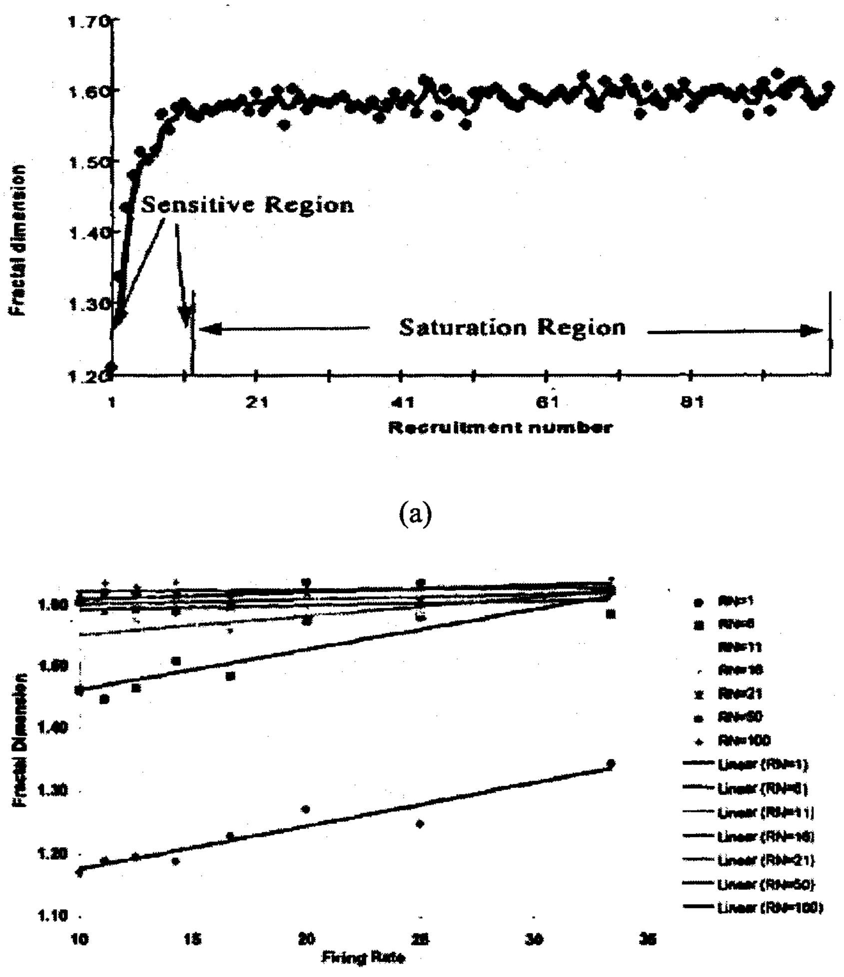

(a)

(b)

Figure 3.4: (a) eFD versus recruitment number and (b) firing rate, reproduced from [11].

It is shown that recruitment is the main determinant of eFD, and the sensitive region and saturation region were proposed to distinguish the two parts of the overall eFD-recruitment relationship [11]. Xiao *et al.* [11] stated, "It is shown that the effects of firing rate highly depends on recruitment level. Firing rate almost doesn't affect eFD at high recruitment. Its influence lies in the sensitive region. The width of the sensitive region and sensitivity are strongly affected by firing rate. A higher firing rate implies a narrower sensitive region, a higher fractal dimension, and thus higher recruitment sensitivity in the region"; however this saturation, which is also seen in the results of Gitter *et al.* [9] (figure 3.3), is likely due to the fact that Box-Counting method's eFD can become saturated for sampled signals (section 2.3.2) [12, 13]. Indeed, the results shown in Figure 3.3 and 3.4 are consistent with the expectation of the Box-Counting eFD saturating at around 1.5 for waveforms [12, 13]. Saturation in Figure 3.3 happens around 1.4 while it is about 1.5 in Figure 3.4. This difference in saturation level can be explained as different signal lengths are used which is 1 s in Figure 3.3 and 12 ms in Figure 3.4. In chapter 4, using simulated data, it is demonstrated that with other methods of computing the eFD, it does not saturate when the number of active MUs and/or their firing rate is increased.

3.2 Muscle Force, Myoelectric Signal Spectrum, and Fractal Dimension

Power spectral analysis of surface MES has been widely used in studying peripheral muscle fatigue [14-17]. During fatigue, there is a shift of the spectral components of the MES towards the lower frequencies (figure 3.5). This shift can be tracked in constant force experiments using the mean frequency (MNF) or median frequency (MDF), which decrease with fatigue [1, 18].

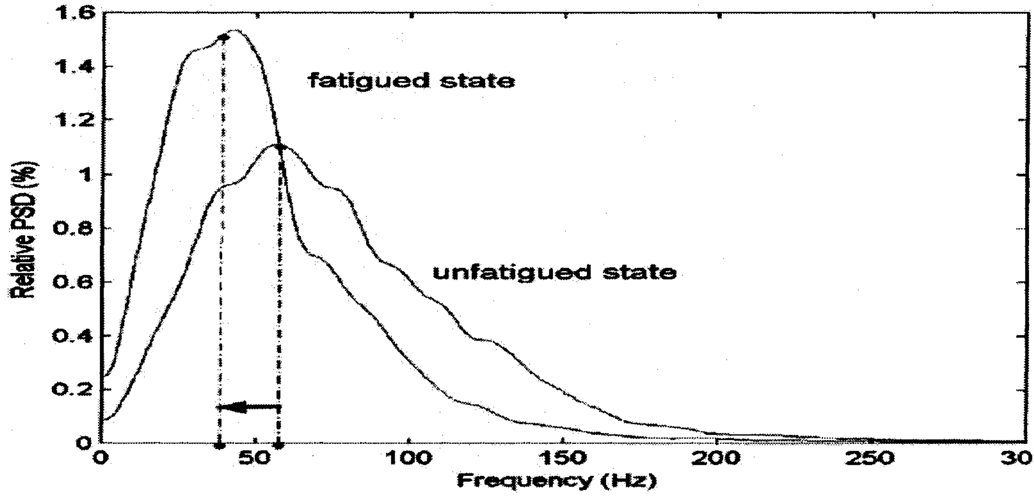

Figure 3.5: MNF or MDF shift to lower frequencies during fatigue, reproduced from [18].

There is an inconsistency about relationship between force and spectral frequencies. The power spectrum of a MES is not significantly influenced by the impulse train that defines the instants of activation of the individual MUs (if there are a sufficient number of independent active MUs); rather, it depends mainly on the shape of the MUAPs. This implies that the power spectrum of MES is not significantly influenced by firing rate [1]. The volume conductor theory [1] indicates that any relationship between recruitment and spectral features can be masked by anatomical or geometrical factors. This means that effects of electrode location should also be considered. Some authors found an increase in MDF and MNF with force level [19, 20], while others showed no increase of these variables with force level [21, 22], and still others observed a decrease of MNF with increasing force [23]. The reasons for such inconsistencies may be related to the experimental technique; that is, the electrode size and placement, the kind of muscle under study, the protocol used to obtain the MNF/MDF-force relationship (ramp or stepwise), the differences in the populations and between the populations, and the signal processing techniques used for power spectrum estimations.

Ravier *et al.* [18] studied force and fatigue effects on the eFI extracted from the power spectrum of MES during short (3 sec) isometric contractions at different strength intensities and during a sustained isometric contraction until exhaustion. In this study, the authors defined the fractal indicator as the slope of the line which is approximating a part of the spectrum with $1/k^{\alpha}$ behavior. In PSM (section 2.3.3), the entire spectrum's shape in a log-log graph is approximated by one line, Figure 2.10 shows PSM applied to a Fractal Noise (FN).

For a log-log graph such as Figure 2.10 in chapter 2, an approximation can be easily done by one line but the power spectrum of MES is not like that. Figure 3.6 shows a typical MES's power spectrum log-log plot.

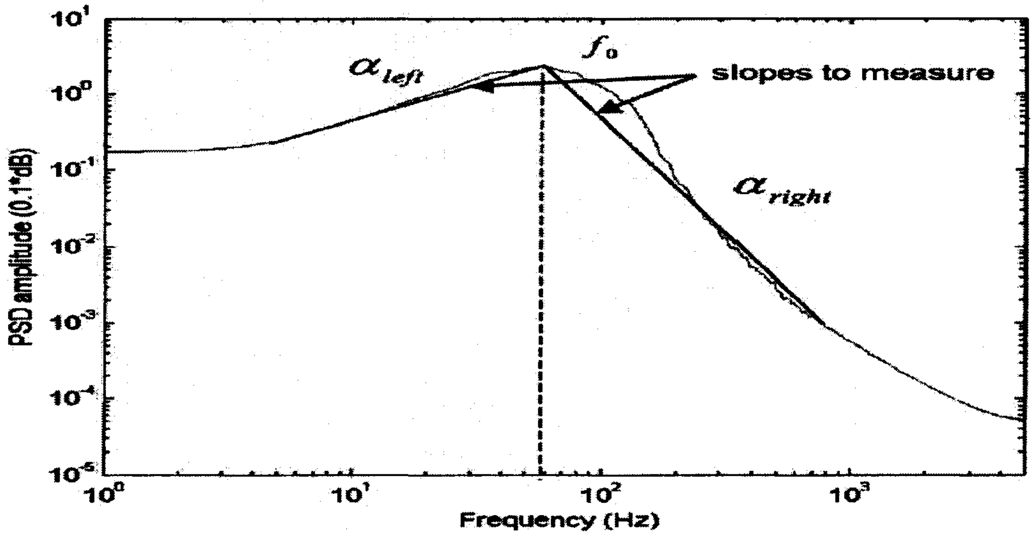

Figure 3.6: Log-Log plot of power spectrum of MES, reproduced from [18].

To approximate the general shape of the MES's power spectrum (having a peak around 50 Hz) a single line like PSM is not suitable. Ravier *et al.* [18] investigated $1/k^{\alpha}$ behavior before and after the maximum frequency (f_0) and defined two fractal indicators, slope of the approximated line for the lower frequencies (left slope; α_{left}) and slope of the approximated line for the upper frequencies (right slope; α_{right}) (figure 3.6). This method will be called second order power spectrum slope method (PSSM) for the reminder of this thesis.

They reported a high correlation between the right slope and muscle force production, while the left hand slope was not as correlated as right hand slope. Results also show MDF is uncorrelated with force (figure 3.7).

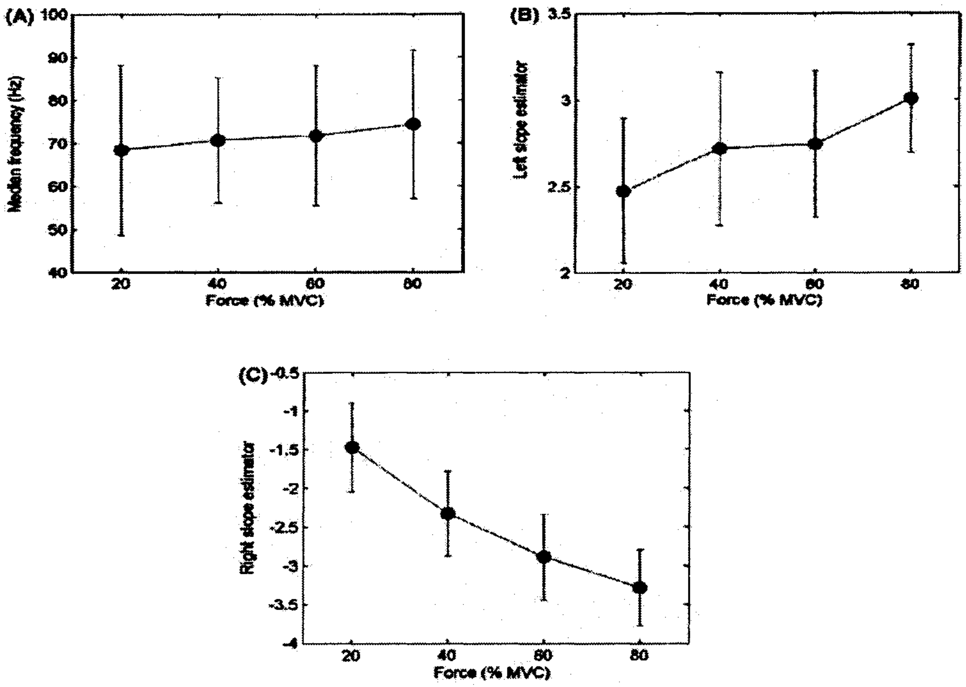

Figure 3.7: (a) MDF vs. force, (b) left slope (α_{left}) vs. force, and (c) right slope (α_{right}) vs. force, reproduced from [18].

This eFI is able to discriminate two levels of force with 95% confidence, when percent difference is at least 20%. [18].

In chapter 4, using simulated surface MES it is shown that increasing depth of recruited MU will cause a decrease in the eFD using time-domain methods, which is mainly caused by attenuation of the tissue filtering. The eFIs, using second order PSSM, is also shown to be highly correlated with the depth of recruited MU and not correlated with number of active MUs and their firing rate which are two main mechanisms that regulate the muscle force.

3.3 General Power Spectrum Method for Myoelectric Signals

General power spectrum model (Eqn 3.1) encompasses the fractal model and other stochastic processes such as the Ornstein-Uhlenbeck and Bermann processes (section 2.3.4) [12, 13].

$$P(k) = \frac{c|k|^{2g}}{(k_0^2 + k^2)^q} \qquad 3.1$$

This model reduces to $P(k) = \frac{c}{|k|^{2q}}$, the model of $1/k^{\alpha}$ behavior, if $g = 0$, $k_0 = 0$ and $1 < q < 2$, which is the same as the PSM. The properties of self similarity and self affinity are satisfied by this general model but in a more restrictive way (Appendix B).

This model has a maximum when,

$$\frac{d}{dk} \ln P(k) = \frac{2g}{k} - \frac{2kq}{k_0^2 + k^2} = 0 \qquad 3.2$$

this implies maximum value of $P(k)$ occurs at frequency k_{max} given by,

$$k_{max} = k_0 \sqrt{\frac{g}{q-g}}, \; q > g \qquad 3.3$$

Complex spectrum of a noise f with a power spectrum like the general RSF model can be written in the form of Eqn 3.4,

$$F(k) = H(k)N(k) \qquad 3.4$$

where $N(k)$ is the complex spectrum of white noise and $H(k)$ is the transfer function,

$$H(k) = \frac{(ik)^g}{(k_0 + ik)^q} \qquad 3.5$$

Beyond the maximum point, the power spectrum decays with a ${}^{1}\!/_{k^{a}}$ behavior. This is consistent with RSF signals and many noise types at the high frequency end of their power spectrum. At high frequencies (k >> k_0), the ${}^{1}\!/_{k^{a}}$ behavior is characterized by the term $\frac{1}{(k_0 + ik)^q}$. At low frequencies (k << k_0) the spectrum is characterized by the term $(ik)^g$. Figure 3.8 shows log-log graph of the power spectrum for varying parameters g, k_0 and q.

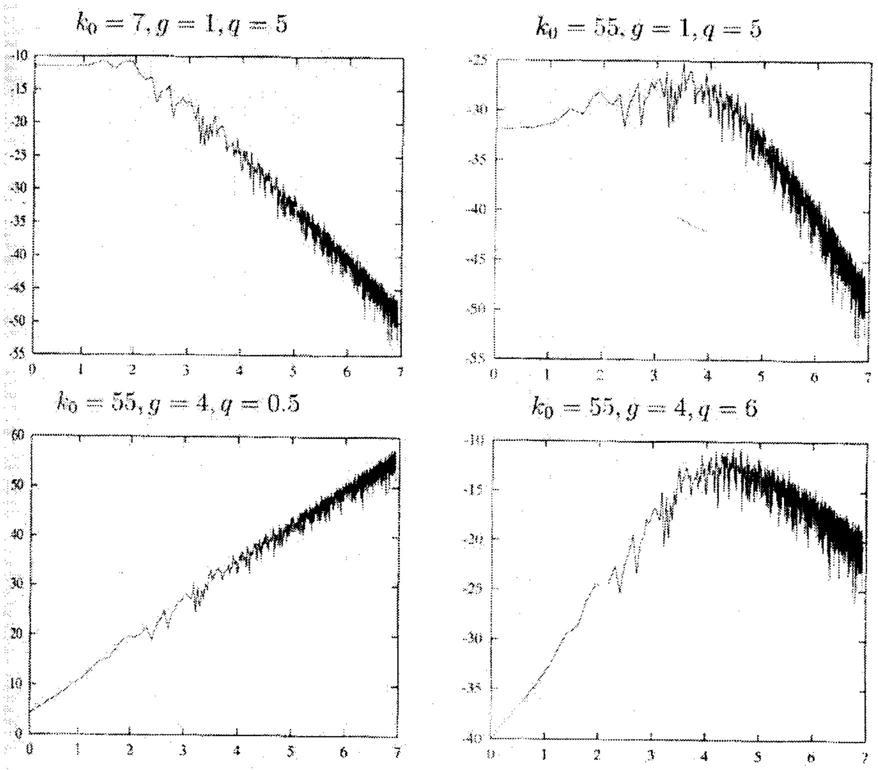

Figure 3.8: Log-log graph of power spectrum for the synthetic noise with varying parameters g, k_0 and q, reproduced from [13].

This model provides a much greater degree of flexibility in terms of characterizing the power spectrum of many noise types, nearly all of which have some degree of statistical self affinity, compared to simple $1/k^{\alpha}$ behavior model which uses a single line.

Figure 3.9 shows a typical log-log graph of MES's power spectrum and the modeled version using GPSM.

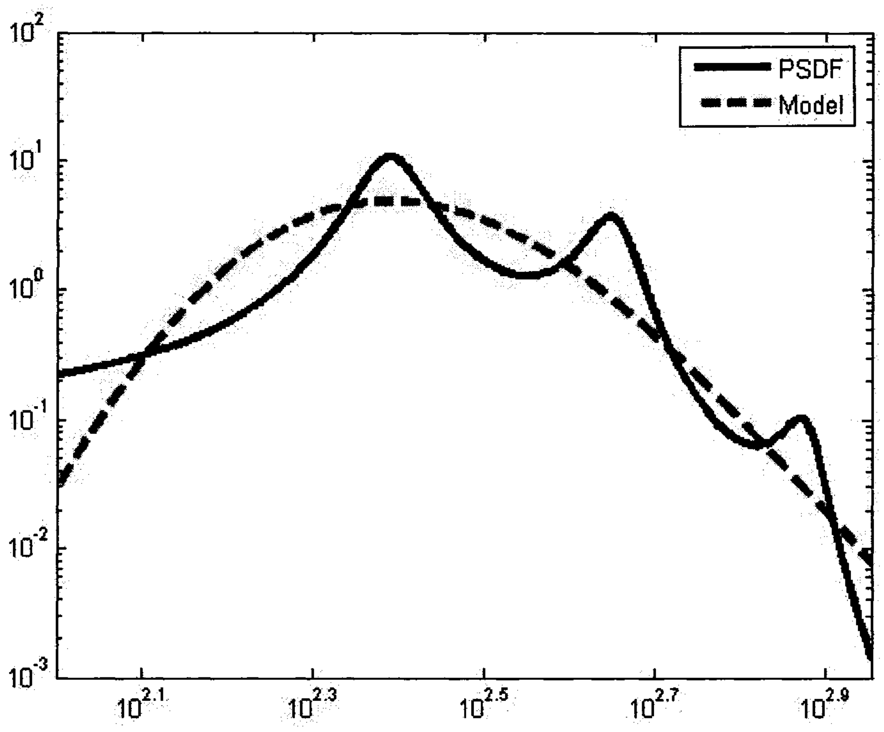

Figure 3.9: Typical log-log graph of MES's power spectrum and the modeled power spectrum of MES using GPSM.

In Figure 3.9 PSD of MES is estimated using the Yule-Walker method with a 9th order autoregressive model. With this order, the model represents a proper MES's PSD and for orders less than 9th, the GPSM does not converge. This general model provides a clearer relationship between the MES parameter and fractal geometry compared to the PSSM and simple spectral slopes. Estimating GPSM parameters using standard least squares divergence happens if there is variability in the power spectrum too. However, it appears that GPSM applied on a Power Spectrum Density (PSD) estimated using a parametric method, which provide a smoother shape, converges. Meanwhile GPSM is not applicable to a PSD estimated using Welch method because it is not smooth enough. An initial value for k_0 could be k_{max} as long as maximum of the MES's PSD is the curve's turning point (slope changes in this point). In case of MESs, limited estimated PSD and data close to this turning point also causes divergence. The k_{max} can be estimated by applying a smoothing process on the power spectrum and for MESs Welch's method can be used. Before k_{max} power spectrum is characterized by g and beyond k_{max} power spectrum is characterized by q. Generally speaking, g and q can be seen as low and high frequency FIs, respectively, similar to the left and right slope method which was used by Ravier *et al.* [18].

References

[1] R. Merletti, P.A. Parker, *Electromyography*. New Jersey: IEEE Press, 2004.

[2] Kukulka C. G and H. P Clamann, "Comparison of the recruitment and discharge properties of motor units in human brachial biceps and abductor pollicis during isometric contractions", Brain Res, Vol.219, 1981 pp. 45-55.

[3] H. S. Milner-Brown and R. B. Stein, "The relation between the surface electromyogram and muscular force", J Phys, Vol.246, 1975 pp. 549-569.

[4] B. Bigland, "The relation between force, velocity and integrated electrical activity in human muscles", J Physiol, Vol.123, 1954 pp. 214-224.

[5] B. Bigland and O. C. J Lipod, “Linear and non-linear surface EMG-force relationships in human muscle”, Am J Physiol Med, Vol.62, 1983 pp. 287-299.

[6] C. J. De Luca and J. H. Lawrence, “Myoelectric signal versus force relationship in different human muscles.” J Appl Physiol, Vol. 54, 1983 pp. 1653-1659.

[7] C.J. Anmuth, G. Goldberg, N.H. Mayer, “Fractal dimension of EMG signals recorded with surface electrodes during isometric contractions is linearly correlated with muscle activation,” *Muscle Nerve*, vol. 17, pp. 953-954, 1994.

[8] M.J. Katz, “Fractals and the analysis of waveforms,” *Comp. Biol. Med.*, vol. 18, pp. 145-156, 1988.

[9] J.A. Gitter, M.J. Czerniecki, “Fractal analysis of the electromyographic interference pattern,” *J. Neurosci. Meth.*, vol. 58, pp. 103-108, 1995.

[10] V. Gupta, S. Suryanarayanan, N.P. Reddy, “Fractal analysis of surface EMG signals from the biceps,” *Int. J. Med. Inform.*, vol. 45, pp. 185-192, 1997.

[11] Z. Xu, S. Xiao, “Fractal dimension of surface EMG and its determinants,” Engineering in Medicine and Biology society, *IEEE Proc.*, vol. 4, 1997, pp. 1570-1573.

[12] M. Al-Akaidi, *Fractal Speech Processing*. Cambridge: Cambridge University Press, 2004.

[13] M.J. Turner, J.M. Blackledge, P.R. Andrews, *Fractal geometry in digital imaging*. London: Academic Press, 1998.

[14] C.J. De Luca, Myoelectrical manifestations of localized muscular fatigue in humans, Crit. Rev. Biomed. Eng. Vol.11 ,1984 pp.251–279

[15] L. Lindstro¨m, I. Peterse´n, Power spectrum analysis of EMG signals and its applications, in: J.E. Desmedt (Ed.), Computer-Aided Electromyography, vol. 10, Karger Basel, 1983, pp.1–51.

[16] W.H.J.P. Linssen, D.F. Stegeman, E.M.G. Joosten, M.A. Van_Hof, R.A. Binkhorst, S.L.H. Notermans, Variability and interrelationships of surface EMG parameters during local muscle fatigue, Muscle Nerve, Vol.16, 1993 pp. 849–856.

[17] R. Merletti, P.A. Parker, *Electromyography*. New Jersey: IEEE Press, 2004.

[18] P. Ravier, O. Buttelli, R. Jennane, P. Couratier, "An EMG fractal indicator having different sensitivities to changes in force and muscle fatigue during voluntary static muscle contractions," *J. Electromyography Kinesiol.*, vol. 15, pp. 210-221, 2005.

[19] B. Gerdle, N. E. Eriksson, "The behavior of mean power frequency of the surface electromyogram in biceps brachii with increasing force and during fatigue. With special regard to electrode distance," Electromyogr Clin Neurophysiol, Vol. 30, 1990 pp. 483-489.

[20] T. Moritani and M. Muro, "Motor unit activity and surface electormyogram power spectrum during increasing force of contraction," Eur J Appl Physiol, Vol. 56, 1987 pp. 260-265.

[21] J. S. Petrofsky and A. R. Lind, "Frequency analysis of the surface EMG during sustained isometric contractions," Eur J Appl Physiol, Vol. 43, 1980 pp. 173-182.

[22] J. T. Viitasalo and P. V. Komi, "Interrelationships of EMG signal characteristics at different levels of muscle tension during fatigue," Electromyogr Clin Neurophysiol, Vol. 18, 1978 pp. 167-178.

[23] M. J. Zwarts, “Evaluation of the estimation of muscle fiber conduction velocity: Surface versus needle method,” Electromyogr Clin Neurophysiol, Vol. 73, 1989 pp. 544-548.

Chapter 4

Effect of MES Parameters on Estimated Fractal Dimension

Simulated MESs permit the investigation of the effects of MES parameters, such as number of active MUs, firing rate, and depth of active motor units, on the measurable variables of the MESs. In this chapter, effects of these three MES parameters on the estimated fractal dimension (eFD) and estimated fractal indicator (eFI) of simulated surface MES using Katz method, Box-Counting method, PSSM and GPSM will be analyzed.

4.1 Structure-Based Surface MES Model

A MU consists of a motor neuron in the spinal cord and the muscle fibers it innervates (figure 4.1).

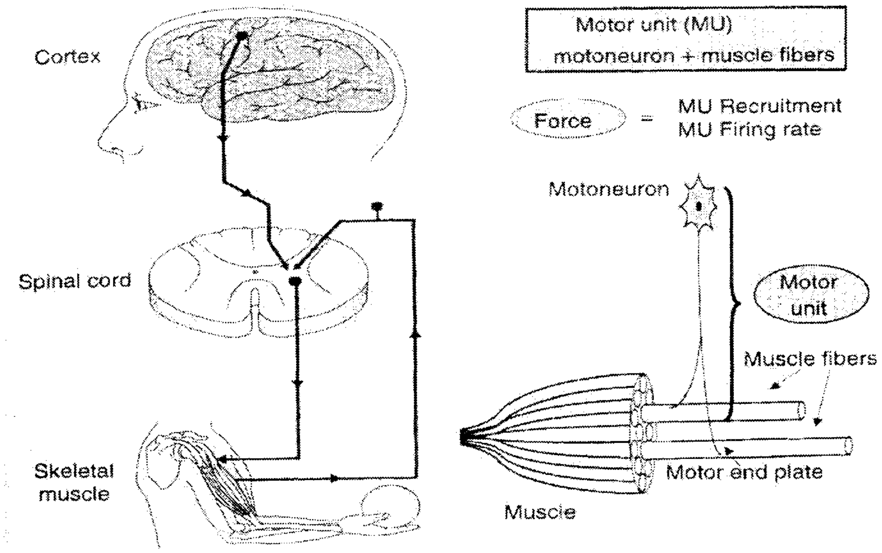

Figure 4.1: A schematic of the MU and its components, reproduced from [1].

An activated muscle fiber produces an electrical depolarization, known as the single fiber action potential (SFAP). SFAPs originate at the motor end plate, which is the point where the motor nerve innervates the muscle fiber, and propagate down the fiber axis. The summation of the SFAPs from the muscle fibers within a motor unit is known as the motor unit action potential (MUAP) [1, 2] (figure 4.2).

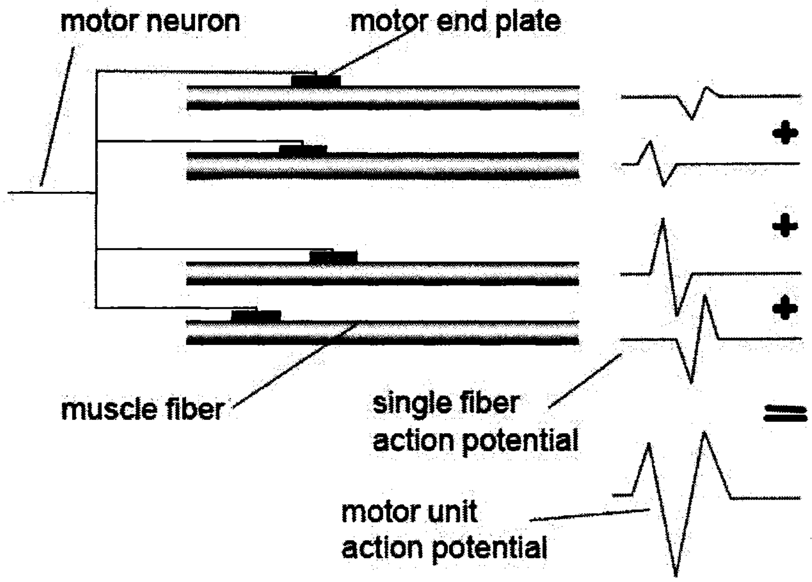

Figure 4.2: Motor unit action potential, reproduced from [2].

Each MUAP has the same wave shape if the measurement geometry remains constant because the action potentials are all-or-nothing phenomena. The MUAP train can be described as the mathematical convolution of the firing instants (a sequence of Dirac functions) with the MUAP wave shape (figure 4.3).

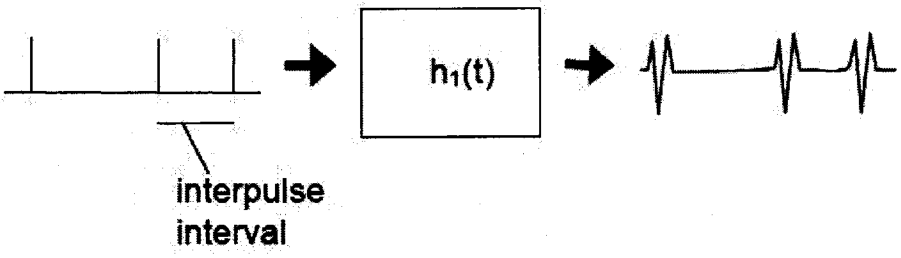

Figure 4.3: Motor unit action potential train, reproduced from [2].

Surface MES can be considered as a signal where the contributions of all active MUs are summed (structure-based model). Contributions of the individual MUs can barely be recognized because of the extensive overlapping when there are a large number of active MUs. Nevertheless, the surface MES's global characteristics are largely dependent on the properties of the contributing MUs such as number of active MUs, firing rate, and depth of active motor units [1]. To model MES, a summation of the MUAP trains can be considered (figure 4.4).

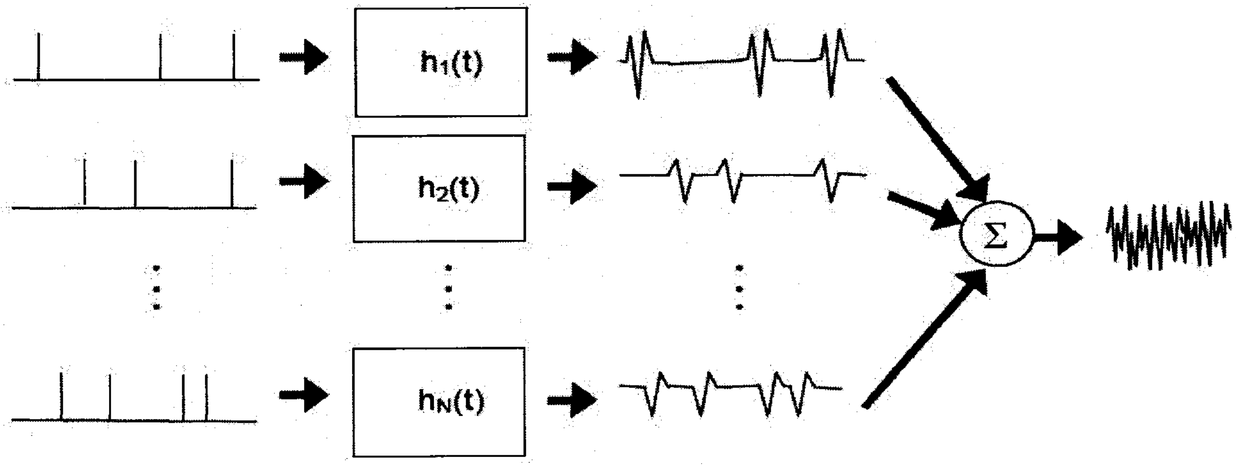

Figure 4.4: Modeling MESs, reproduced from [2].

The MUAP characteristics such as shapes and distribution of amplitude and duration, are determined by morphological and functional properties of the activated MUs, together with passive and active properties of the sources and surrounding tissue (volume conductor) [1]. Figure 4.5 shows a possible approach to a structural model. The MESs in this chapter are also simulated using a structural model using the MES simulator by Jiang [3]. Surface Single Fiber Action Potential (SSFAP) at the recording point is provided as Eqn 4.1 [4],

$$SSFAP(t,v) = K_1 \cdot s(t) * \left[h_L(t,d,r,l_L,v) + h_R(t,d,r,l_R,v) \right] \qquad 4.1$$

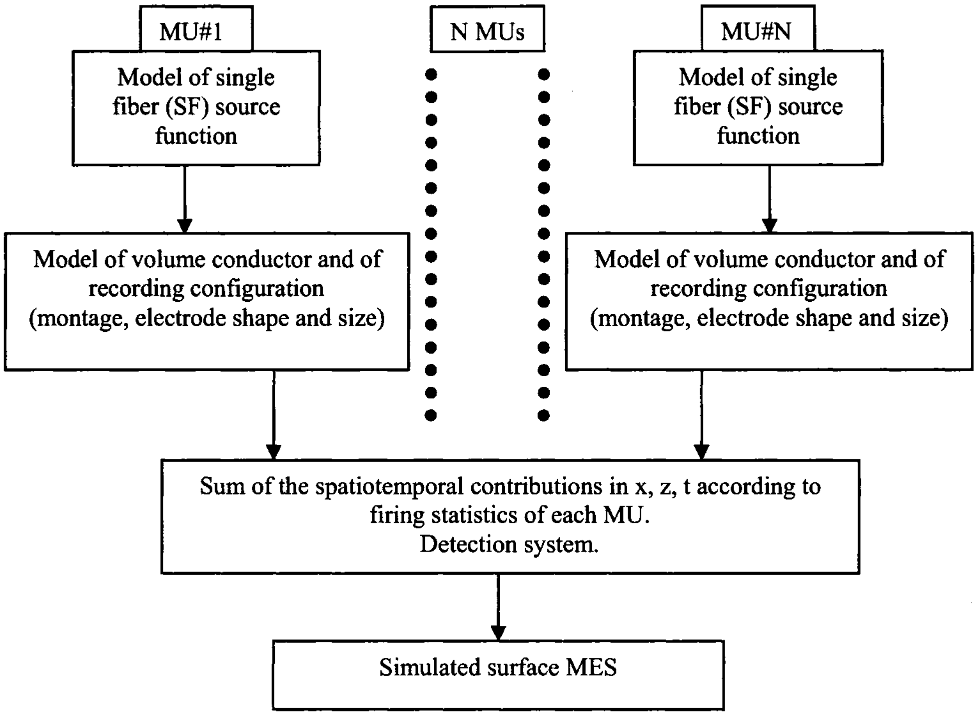

Figure 4.5: Structural MES modeling, reproduced from [1].

where $K_1=(1/2)\left(\sigma_i\theta^2/4\sigma_e\right)$ is a constant, σ_i and σ_e are the intracellular and extracellular conductivities, $\theta=a/v$, a is the fiber radius, and v is the propagation velocity; $s(t)=\left(\delta V_m(t)/\delta t\right)$ is the first derivative of the transmembrane potential, which is taken as the source; $*$ is the convolution operator acting over time; h_L and h_R are left-side and right-side tissue filter impulse response functions which are given by Eqn 4.2 and 4.3,

$$h_L\left(t,d,r,l_L,v\right)=\begin{cases}0 & t<0\\ h\left(t+\dfrac{d}{v}\right) & 0\le t\le t_L\\ 0 & t>t_L\end{cases} \qquad 4.2$$

$$h_R(t,d,r,l_R,v) = \begin{cases} 0 & t < 0 \\ h\left(t - \frac{d}{v}\right) & 0 \le t \le t_R \\ 0 & t > t_R \end{cases} \qquad 4.3$$

where

$$h(t) = \frac{t}{\left[\left(\frac{r}{v}\right)^2 \left(\frac{\sigma_l}{\sigma_t}\right) + t^2\right]^{3/2}} \qquad 4.4$$

r is the fiber depth underneath the recording electrode; d axial distance from the innervation point to the recording point; σ_l and σ_t longitudinal and transversal conductivities; $t_L = l_L/v$; $t_R = l_R/v$ and l_L and l_R are distances from the innervation point to the left and right fiber terminations, respectively. Surface MUAP (SMUAP) recorded at the skin surface can be found as the sum of the contributions of all M fibers activated within the MU (Eqn 4.5),

$$SMUAP(t,v) = \sum_{i=1}^{M} SSFAP_i(t,v) \qquad 4.5$$

The SMUAP waveforms generated by this model are in a good agreement with experimental surface MES [3]. The MES can be found as the sum of all N SMUAPs.

$$MES = \sum_{N} SMUAP \qquad 4.6$$

4.1.1 Simulated MESs

Simulated MES used in this chapter was produced using a structural model simulation program by Jiang [3] for 1200 ms in five different sets. Table 4.1 summarizes the simulation parameters.

Table 4.1: Simulation parameters

Number of electrodes	Interval between electrodes	Source duration	Length of fiber	Number of fibers in MU
2	5 mm	3 msec	Left 120 mm Right 90 mm	10

Sample rate	Conduction velocity	Termination dispersion	Innervation zone (IZ) dispersion	Distance from (IZ) to electrode
20 kHz	Mean=6 m/sec Standard deviation=3 m/sec	Standard deviation=3 mm	Standard deviation=3 mm	35 mm

4.2 Relationships Between Number of Active MUs, firing rate and eFD

As it was previously stated (section 3.1), the main mechanisms of regulating muscle force are the recruitment of additional MUs and increase of firing rate of already active MUs. There is a wide variability between muscles with MU recruitment and with MU firing rate coding in obtaining the required muscle force. These differences are related to muscle's size and composition. This also means these two mechanisms (i.e. recruitment number and firing rate) are present in different proportions in different muscles [1]. It is well established that an increase in recruitment number and firing rate will cause an increase in the MES's amplitude. Figure 4.6 and 4.7 shows the mean Root Mean Square (RMS) voltage of simulated surface MES from five different sets for different number of MUs and firing rates with MUAP parameters according to table 4.1.

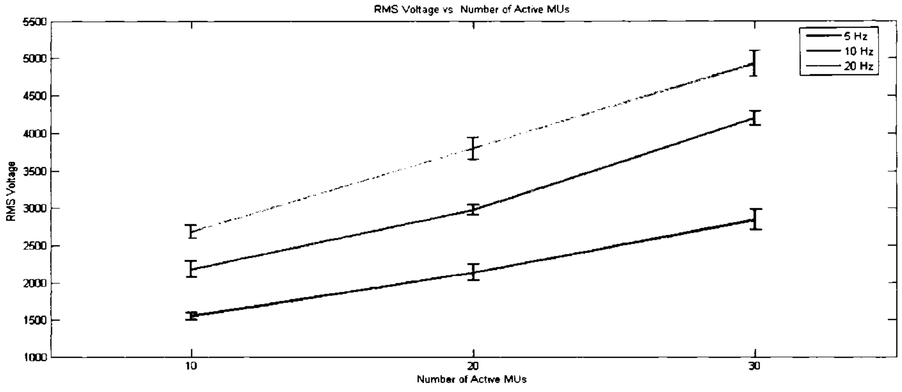

Figure 4.6: Mean RMS voltage and standard deviation from five sets vs. number of active MUs for different firing rates.

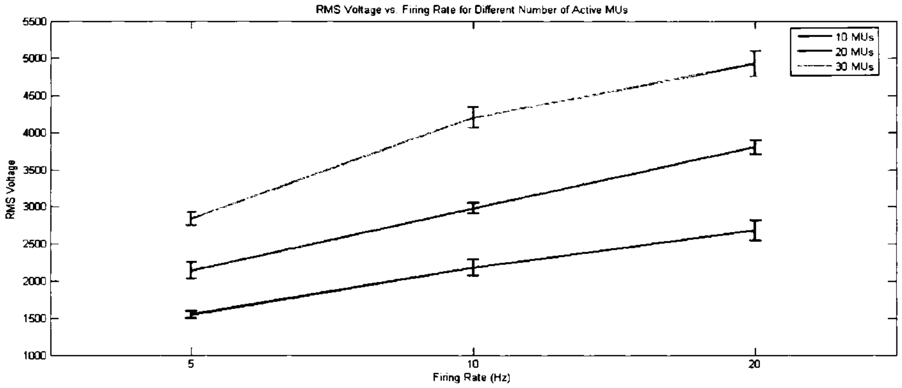

Figure 4.7: Mean RMS voltage and standard deviation from five sets vs. firing rate for different number of active MUs.

Figure 4.8 and 4.9 show eFD using Katz and Box-Counting methods versus number of active MUs for different firing rates. To estimate the fractal dimension using Box-Counting method the curve of the simulated MESs was covered by square boxes with side length of size $\frac{1}{2^n}$. The n indicates the recursion's number which was an integer between 1 and 8 for this study. An increase in the amplitude will cause an increase in the eFD using time-domain methods because it will increase the area occupied by the curve of the signal (section 2.3.1). The Katz method exhibits a behavior similar to the RMS voltage. The Box-Counting method, also exhibits a similar behavior, which is not as linear. The discrepancy can be explained by the saturation of this method near 0.6 above the topological dimension which was discussed in section 2.3.2 and is the main problem for the Box-Counting method.

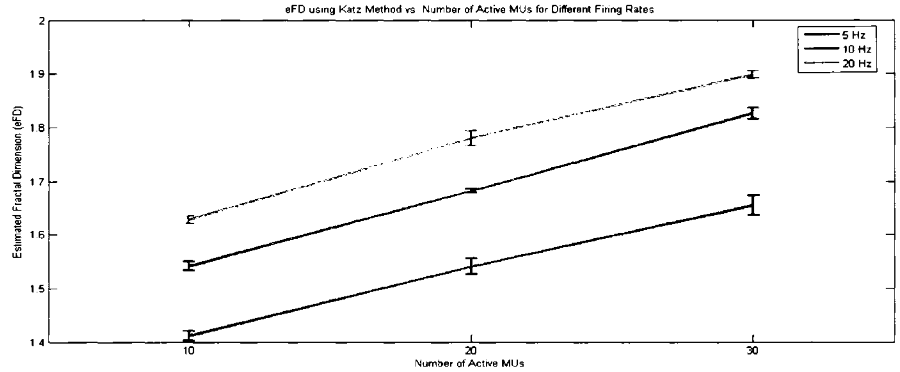

Figure 4.8: Mean eFD and standard deviation using Katz method from five sets vs. number of active MUs for different firing rates.

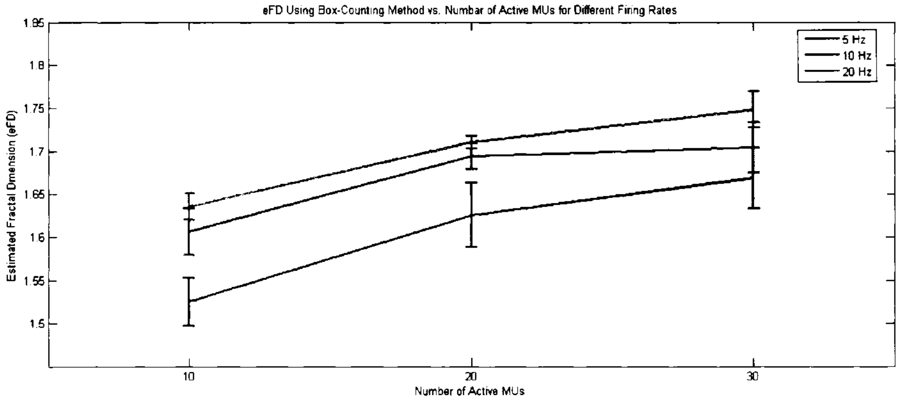

Figure 4.9: Mean eFD and standard deviation using Box-Counting method from five sets vs. number of active MUs for different firing rates.

The $1/k^{\alpha}$ behavior in the power spectrum of simulated data is investigated using the PSSM, computing the slope of the approximated line for the lower frequencies (left slope; α_{left}) and slope of the approximated line for the upper frequencies (right slope;

α_{right}) (section 3.2). Figure 4.10 and 4.11 are plots of α_{right} and α_{left} as function of the number of active MUs and firing rate. For PSSM the peak frequency (i.e. frequency of the power spectrum's maximum) was determined by estimating the power spectrum using the Welch method with a Hamming window of length 500 ms and 50 % overlap between windows. The Yule-Walker method, with a 6th order autoregressive model, was used for estimating the power spectrum, which is used for solving the least squares in order to obtain right and left hand slopes (i.e. α_{left} and α_{right}) of the second order PSSM. As it was mentioned earlier in section 3.2, the power spectrum of MES is not significantly influenced by firing rate [1]. In the same line according to volume conductor theory [1] effects of recruitment number and number of active MUs on these spectral features of MES are negligible; however, it is unarguable that as the number of active MUs and/or firing rate are increased power of the signal is increased, hence area under curve of the power spectrum of MES increases as the total power of the signal increases. This means changes to the power spectrum shape might be hardly traceable by eFI using PSSM in order of slope of the approximated line for the lower frequencies (left slope; α_{left}) and slope of the approximated line for the upper frequencies (right slope; α_{right}). This can be explained as follows, when area under the power spectrum is increased all points of the power spectrum curve tend to shift upwards and changes to the slope of the approximated line is not significant (figure 4.12).

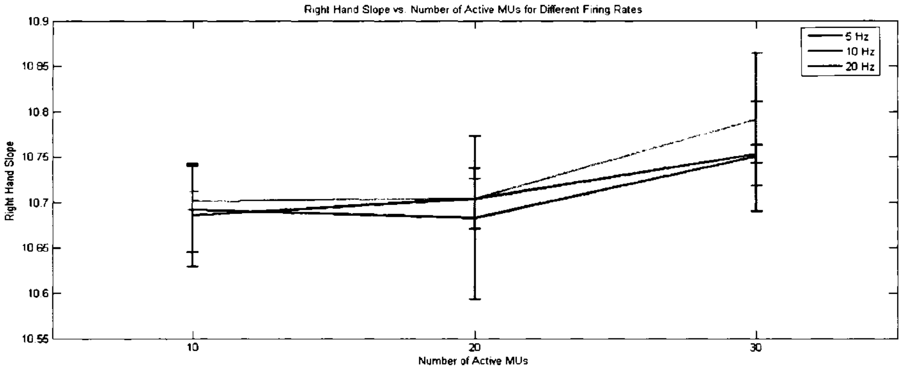

Figure 4.10: Mean slope and standard deviation of the approximated line for the upper frequencies (right slope; α_{right}) from five sets vs. number of active MUs for different firing rates.

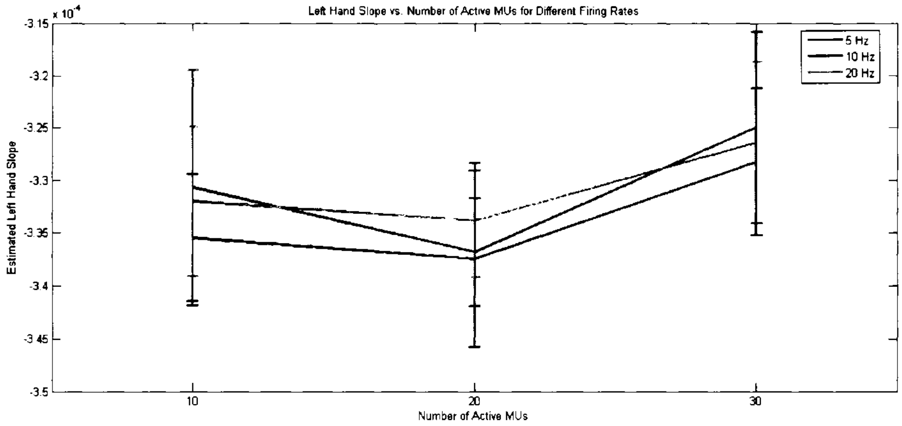

Figure 4.11: Mean slope and standard deviation of the approximated line for the lower frequencies (left slope; α_{left}) from five sets vs. number of active MUs for different firing rates.

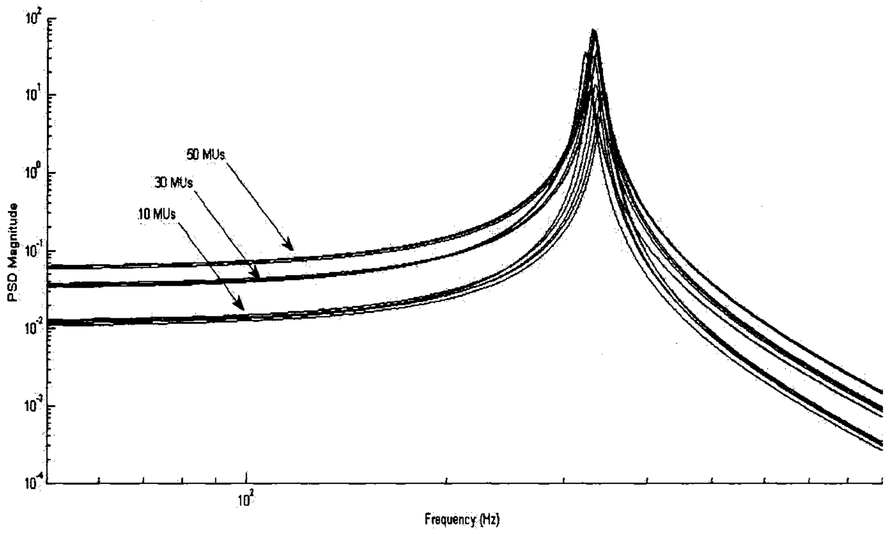

Figure 4.12: Changes of the area under power spectrum curve with the number of active MUs.

Figure 4.10 and 4.11 show changes in the slopes are negligible due to the fact that power spectrum shape and distribution of frequencies are not greatly affected by number of active MUs and firing rate. As shown in Figure 4.12, with increasing number of MUs, the power spectrum does increase but the shape does not change much.

Figure 4.13, 4.14 and 4.15 show estimated fractal indicators q and g using GPSM. The Yule-Walker method, with a 9th order autoregressive model, was used for estimating the power spectrum, which is used for solving the least squares in order to obtain GPSM's parameters (i.e. q and g).

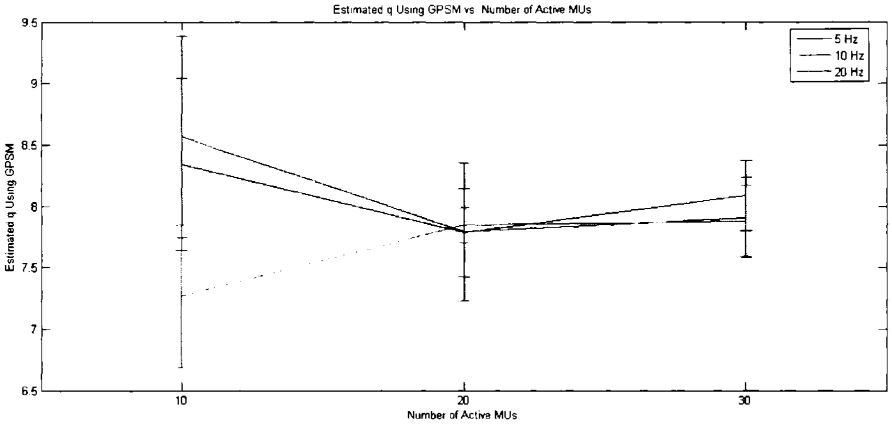

Figure 4.13: Mean estimated fractal indicator for upper frequencies q and standard deviation using GPSM from five sets vs. number of active MUs for different firing rates.

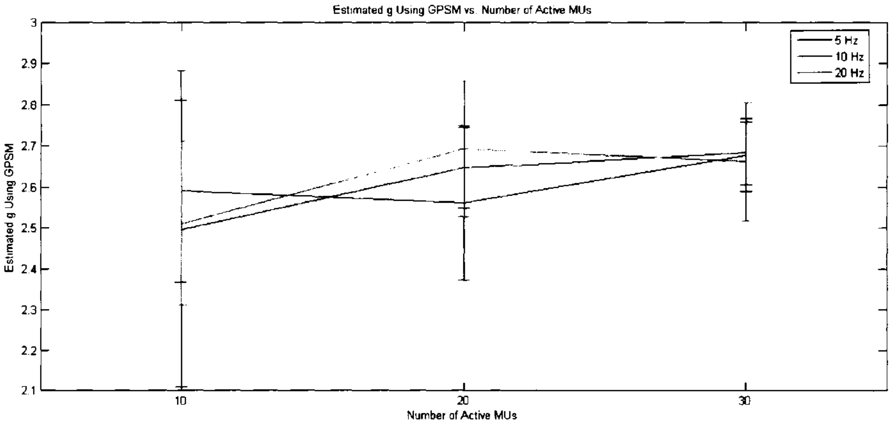

Figure 4.14: Mean estimated fractal indicator for lower frequencies g and standard deviation using GPSM from five sets vs. number of active MUs for different firing rates.

Both GPSM parameters (i.e. q high frequency indicator and g low frequency indicator) show small changes with the number of active MUs and firing rate. This behavior is consistent with PSSM results and can be explained with small changes of power spectrum shape and distribution of frequencies due to the changes in spatial and temporal recruitment.

4.3 Relationships Between Depth of Active MUs and eFD

The amplitude, and hence RMS voltage, of the MES will decrease with an increased depth of the recruited MU caused by the tissue filtering attenuation (figure 4.16). The eFD computed by Katz and Box-Counting methods, which are highly correlated with the RMS voltage, would therefore decrease as well. This is demonstrated for the Katz method in Figure 4.17 and the Box-Counting method in Figure 4.18. Again, the saturation of Box-Counting method at about 1.6 has effected the results (section 3.2.3).

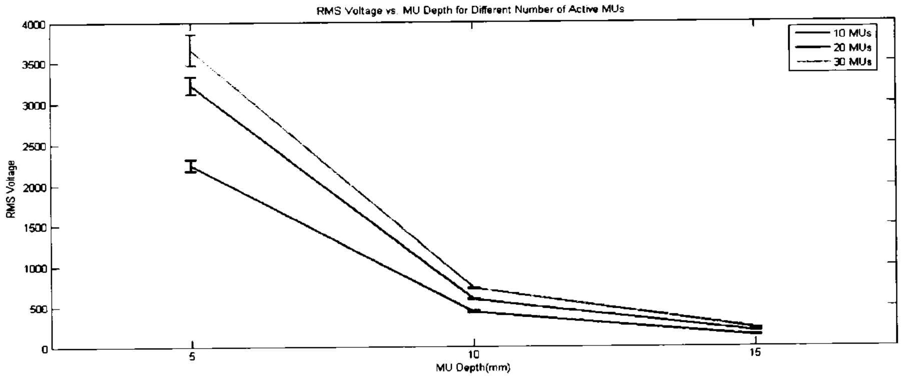

Figure 4.16: Mean RMS voltage and standard deviation from five sets versus depth of active motor units for different number of active MUs.

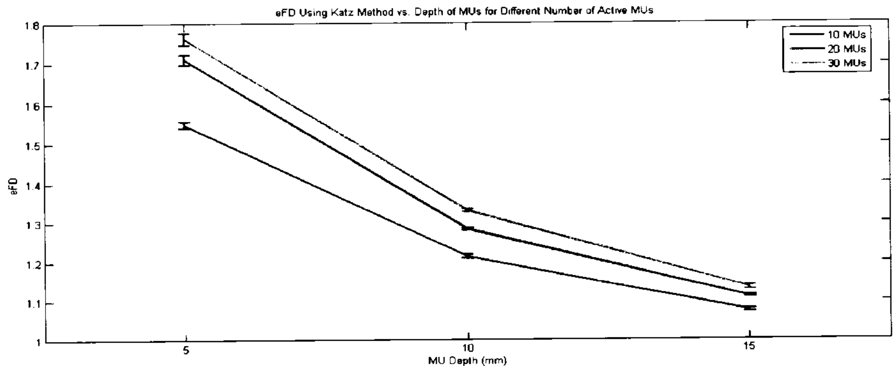

Figure 4.17: Mean eFD and standard deviation using Katz method from five sets versus depth of active motor units for different number of active MUs.

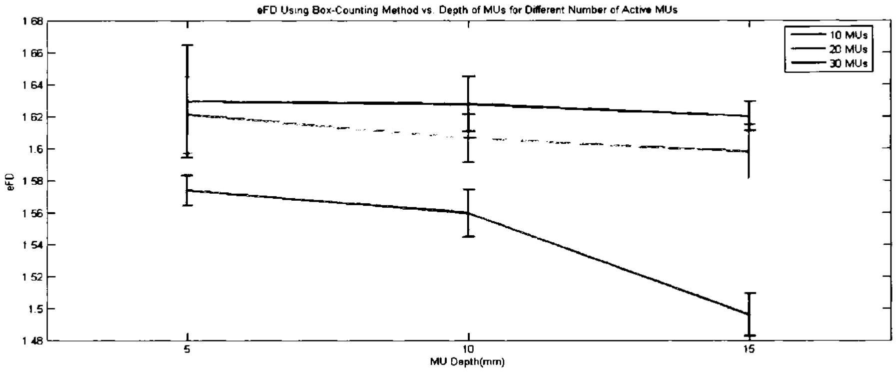

Figure 4.18: Mean eFD and standard deviation using Box-Counting method from five sets versus depth of active motor units for different number of active MUs.

Depth of the recruited MU will affect the frequency content of MES and hence the power spectrum shape. When a deep MU is recruited it will contribute more to the lower frequency region of the MES power spectrum because of the low-pass filtering nature of the surrounding tissue (tissue filtering).

Figure 4.19 and 4.20 show estimated slope of the approximated line for the lower frequencies (left slope; α_{left}) and slope of the approximated line for the upper frequencies (right slope; α_{right}) versus different MU depths for different number of active MUs.

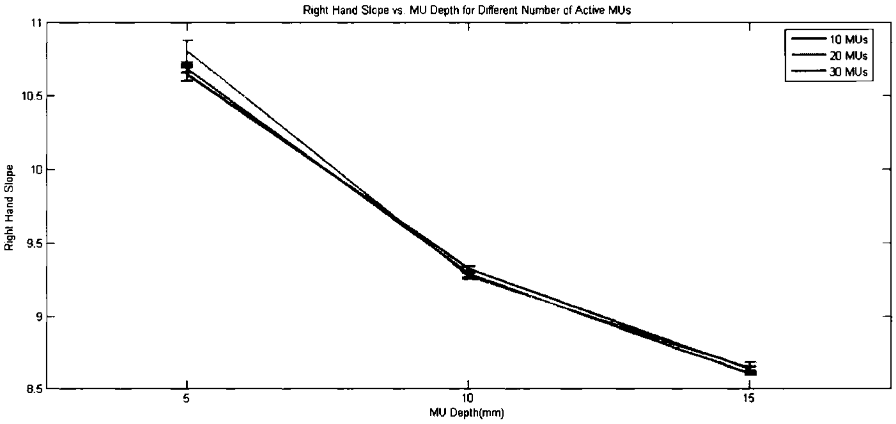

Figure 4.19: Mean slope and standard deviation of the approximated line for the upper frequencies (right slope; α_{right}) vs. depth of active motor units for different number of active MUs.

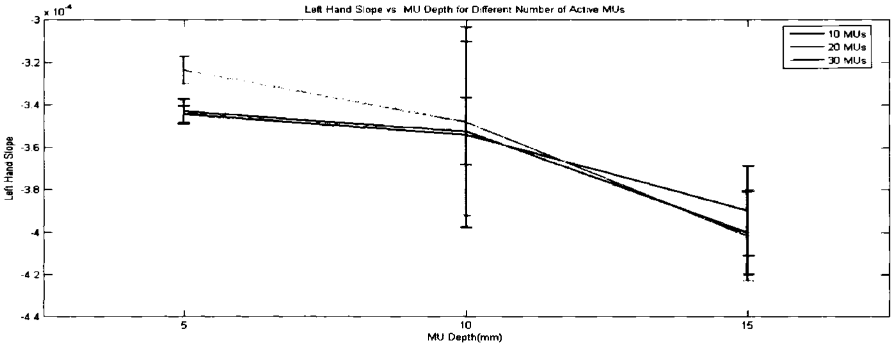

Figure 4.20: Mean slope and standard deviation of the approximated line for the lower frequencies (left slope; α_{left}) vs. depth of active motor units for different number of active MUs.

Both slopes are decreased as the MU depth is increased, especially the right hand slope (α_{right}) which is highly correlated with MU depth. Right hand slope gives a valuable measure for the MU depth, independent of number of active MUs and firing rate, which cause a much smaller change in the slope relative to the MU depth.

Figure 4.21, 4.22 and 4.23 show estimated fractal indicators q and g (chapter 2) using GPSM for different MU depths. Both parameters show a high correlation with the MU depth. These changes in GPSM's parameters are also consistent with PSSM results and the fact that depth of active MUs effects frequency content of MESs.

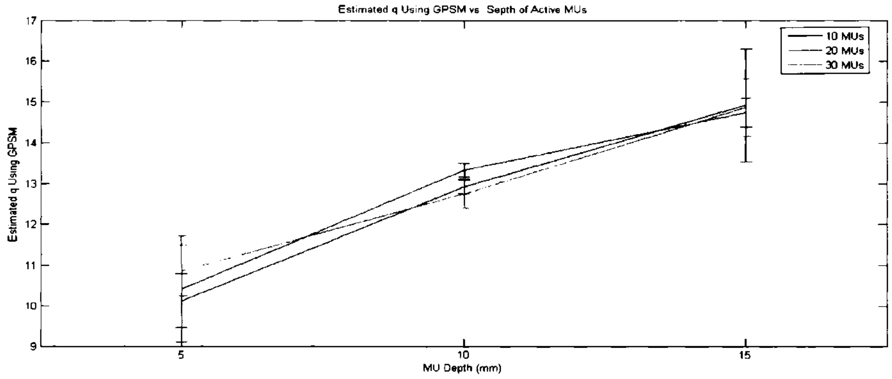

Figure 4.21: Mean estimated fractal indicator for upper frequencies q and standard deviation using GPSM vs. depth of active motor units for different number of active MUs.

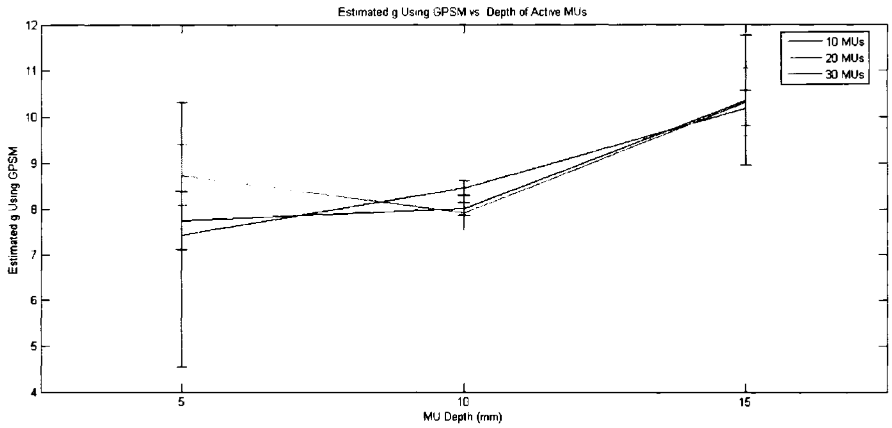

Figure 4.22: Mean estimated fractal indicator for lower frequencies *g* and standard deviation using GPSM vs. depth of active motor units for different number of active MUs.

4.4 Summary

Table 4.1 show the quantified significance (*p*-values) using ANOVA which was performed in SPSS [6] for the effects of number of active MUs, firing rate and depth of active MUs on eFD using Katz method and Box-Counting method and eFI using PSSM and GPSM. These values are compared to a level of significance (α_T=0.05). Values below this threshold show a significant effect and values higher than the threshold show insensitivity, with significance highlighted in bold.

Table 4.2: ANOVA of MES parameters (*p*-values with signficant effects shown in bold; $\alpha_T = 0.05$)

Method/Parameter	Number of Active MUs	Firing Rate	MU Depth
RMS Voltage	**< 0.001**	**< 0.001**	**< 0.001**
Katz Method	**< 0.001**	**< 0.001**	**< 0.001**
Box-Counting Method	**0.002**	**< 0.001**	**< 0.001**
PSSM, Right Slope	0.354	0.096	**< 0.001**
PSSM, Left Slope	0.248	0.357	**0.011**
GRSFM, Upper Frequency Indicator *q*	0.223	0.436	**0.002**
GRSFM, Lower Frequency Indicator *g*	0.117	0.200	**0.011**

According to table 4.2 Katz and Box-Counting methods results are sensitive to all three parameters, which are consistent with effects of number of active MUs, firing rate and depth of active MUs on amplitude and RMS voltage of the MES. Meanwhile changes caused by these three MES's parameters on the eFD are more or less with the same order of magnitude.

The eFIs using PSSM and GPSM are not sensitive to number of active MUs and firing rate while they are significantly sensitive to depth of active MUs. This is consistent with insensitivity of the shape power spectrums to the number of active MUs and firing rate and sensitivity of power spectrum to depth of active MUs. Moreover changes due to the depth of active MUs are much larger than changes due to the number of active MUs and firing rate.

This implies that the power spectrum-based methods (i.e. PSSM and GPSM) could potentially be used as a quantitative measure that is not largely affected by force (i.e. number of active MUs and firing rate).

References

[1] R. Merletti, P.A. Parker, *Electromyography*. New Jersey: IEEE Press, 2004.

[2] Adrian D.C. Chan, "Multi-expert automatic speech recognition system using myoelectric signals," Ph.D. dissertation, University of New Brunswick, New Brunswick, Canada 2002.

[3] N. Jiang, "Modelling of motor unit innervation process correlation and motor unit common drive in human skeletal muscles," M.Sc.E. Thesis, University of New Brunswick, Fredericton, New Brunswick, Canada, 2004.

[4] Jose A. Gonzalez-Cueto and Philip A. Parker, "Deconvolution estimation of motor unit conduction velocity distribution," IEEE Trans Bio Eng, Vol.49, Sept.2002 pp. 955-962.

[5] B. B. Mandelbrot, “Fractal Geometry of Nature”, Freeman-Oxford press 1983.

[6] www.SPSS.com

Chapter 5

Isometric Constant Force Contractions

In this chapter, estimated fractal dimensions (eFD) and estimated fractal indicators (eFI) during Isometric Constant Force Contractions (ICFC) for different force levels and joint angles are analyzed. This expands previous research on MES fractal parameters, which have thus far only examined force effects. First, effects of muscle length (joint angle) on the produced force are described. Second, experimental results during ICFC for different force levels and joint angles are presented.

5.1 Length-Tension Relationship in Skeletal Muscles

A number of factors influence the strength of a muscle contraction (muscle force) including: the number of fibers within the muscle, the radius of each muscle fiber, and the length of the muscle fibers. There is an optimal length for muscle fibers at which they can generate maximum force [1]. An increase or decrease in muscle (and sarcomere) lengths from this optimal length results a decline in the capacity of muscle to produce force (figure 5.1). This relationship can be mainly explained in terms of the sliding filament mechanism and their overlap which affects number of cross bridges in the overlap region and hence the produced force [1].

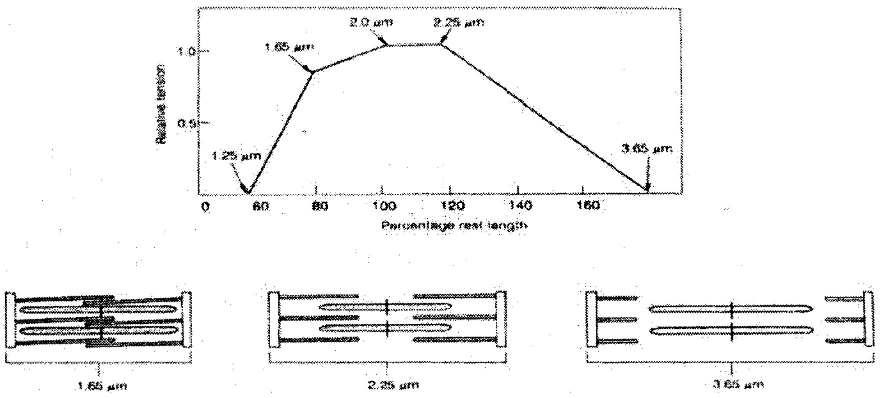

Figure 5.1: Variation in relative produced tension with muscle fiber length, reproduced from [1].

For ICFC at different joint angles, length of the muscle fibers are different; therefore, it is reasonable to see different recruitment of MUs and firing rate strategies to produce the same amount of force at different joint angles (and muscle lengths). It is expected that there would be a lower number of active MUs and/or lower firing rates at the optimal muscle length or optimal joint angle, where muscle has the capacity of producing more force compared to other joint angles.

5.2 Fractal Indicators During ICFC

During ICFC with different joint angles it is expected to see lower amplitudes at joint angles where the length of the muscle is closer to optimal length and hence a lower eFD using time domain estimation methods (i.e. Katz and Box-Counting). Moreover, the depths of the active MUs are also changed because of the changing geometry of the measurement (e.g. tissue stretching) and it is expected to see a change in the fractal indicators using spectrum based methods (i.e. PSSM and GPSM) too. Changes in depth of the active MUs will also affect the eFD using time domain methods (section 4.3) and therefore make it impossible to discern force and joint angle effects. To analyze relationships of eFD and eFI of the MES and joint angle, an experiment was performed on *biceps brachii* during ICFC at different joint angles.

5.2.1 Data Acquisition Equipment

Data were collected according to the Tri-Council policy for *Research Involving Human Subjects* [5]. The experiment was reviewed and approved by the Carleton University Research Ethics Committee (Appendix C). A group of five healthy males participated in this study (age range 22 to 29; average age 25). MESs were collected from belly of the *biceps brachii* using surface electrodes in a bipolar configuration using Ag-AgCl Duotrode electrodes (Myotronics, 6140) spaced 1.9 cm apart and an Ag-AgCl Red Dot electrode (3M, 2237) as a reference electrode placed on elbow (figure 5.2). Signals were amplified using a Grass-Telefactor amplifier (M15A54) with variable gains between 10 to 100, such that the maximum dynamic range of the analog-to-digital converter was utilized without over ranging, and filtered with a bandwidth of 1 Hz to 300 Hz. MESs were then sampled at 1000 Hz using a 12-bit analog-to-digital converter board (National Instruments, PCI-6071E).

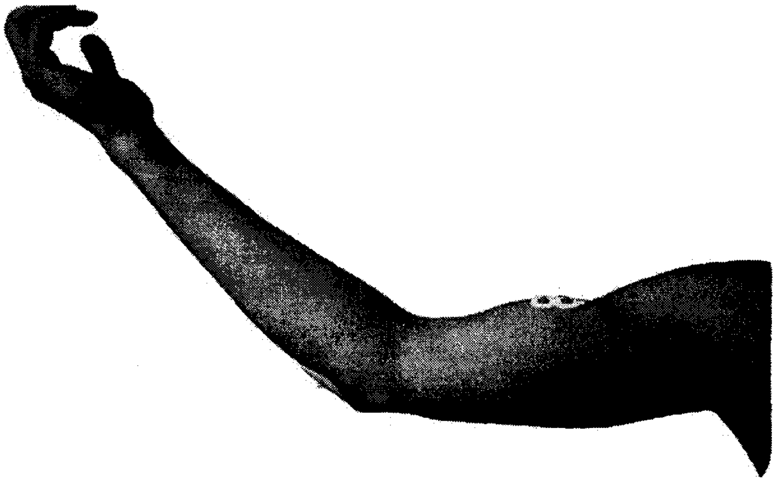

Figure 5.2: Electrode placement.

5.2.2 Data Acquisition Protocol

The data acquisition protocol consists of four elbow joint angles: 60°, 90°, 120° and 150°, where 180° is considered full elbow extension. Joint angle of right arm was kept constant using a customized apparatus (figure 5.3 and 5.4) and force was also regulated by two different weights to produce torque across the main wheel and hence orthogonally to the forearm.

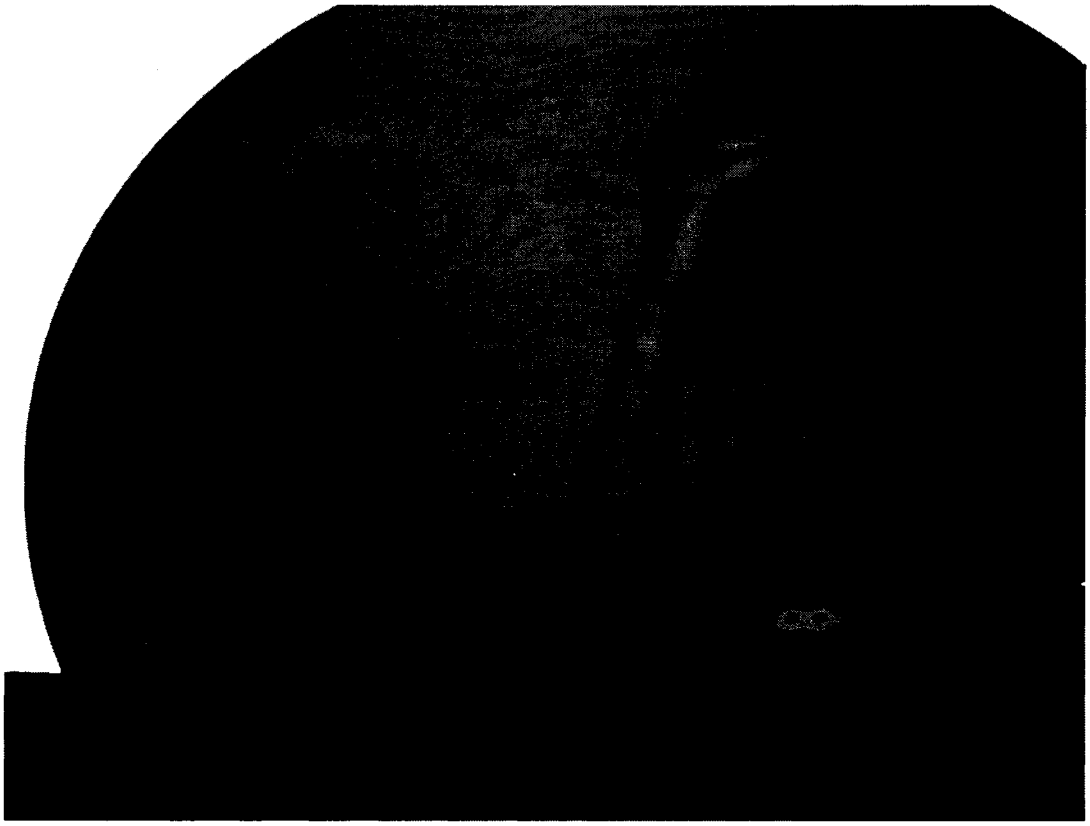

Figure 5.3: Apparatus set at 90° angle.

The weights were 5 lb (2.27 kG) and 7.5 lb (3.41 kG), requiring a force of 31 N and 47 N on the handle, respectively, to maintain a constant angle[1]. The apparatus was constructed considering the average forearm length of the subjects.

Each contraction was kept for 15 seconds and there was a minimum of a 1 minute rest between each trial to avoid fatigue. Joint angle-force combinations were randomized to avoid ordering effects. Each subject performed ICFC in all eight joint angle-force combinations of joint angle-force three times.

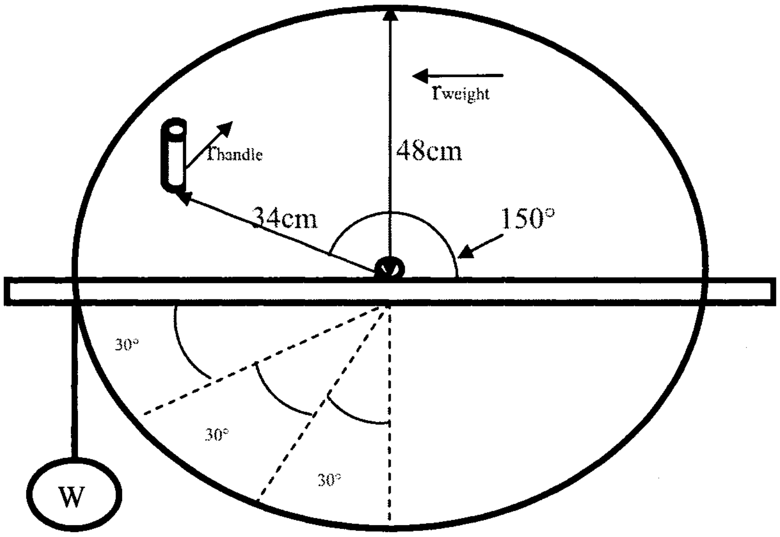

Figure 5.4: Schematic of apparatus set at a 150° angle.

---

[1] The torque at the handle should equal the torque caused by the weight to maintain a particular joint angle

$\tau_{\mathbf{weight}} = \tau_{\mathbf{handle}}$; therefore, $\mathbf{F}_{\mathbf{handle}} = \dfrac{\mathbf{mass}_{\mathbf{weight}} \times \mathbf{a}_{\mathbf{gravity}} \times \mathbf{r}_{\mathbf{weight}}}{\mathbf{r}_{\mathbf{handle}}}$

5.2.3 Processing

The eFD was computed using the Katz method and Box-Counting method, and the eFI was computed using the PSSM. To estimate the fractal dimension using Box-Counting method the curve of the MESs was covered by square boxes with side length of size $\frac{1}{2^n}$. The n indicates the recursion's number which was an integer between 1 and 8 for this study. For PSSM the peak frequency (i.e. frequency of the power spectrum's maximum) was determined by estimating the power spectrum using the Welch method with a Hamming window of length 500 ms and 50 % overlap between windows (smoothing process on power spectrum). The Yule-Walker method, with a 6th order autoregressive model, was used for estimating the power spectrum, which is used for solving the least squares in order to obtain right and left hand slopes (i.e. α_{left} and α_{right}) of the PSSM. GPSM was also considered, however results do not converge in most cases. This is mainly caused by variability in the power spectrum and effects of the 60 Hz line filter. These problems are further addressed in section 5.2.4.5.

5.2.4 Results

5.2.4.1 RMS Voltage vs. Joint Angle

Figure 5.5 and table 5.1 show the average RMS voltages of three trials versus joint angle for all subjects and Figure 5.6 show average results for all subjects. Average RMS voltage of MES is higher for the 7.5 lb weight compared to 5 lb weight torque for all subjects, which is consistent with the fact that the recruitment number and firing rate are increased. Average RMS voltage for all subjects is also consistent with the length-tension relationships of a muscle. Less amplitude at 120° and 90° compared to 60° and 150°

implies muscle length is closer to optimal length in these joint angles (figure 5.5). Changes due to joint angle are more noticeable for the higher weight.

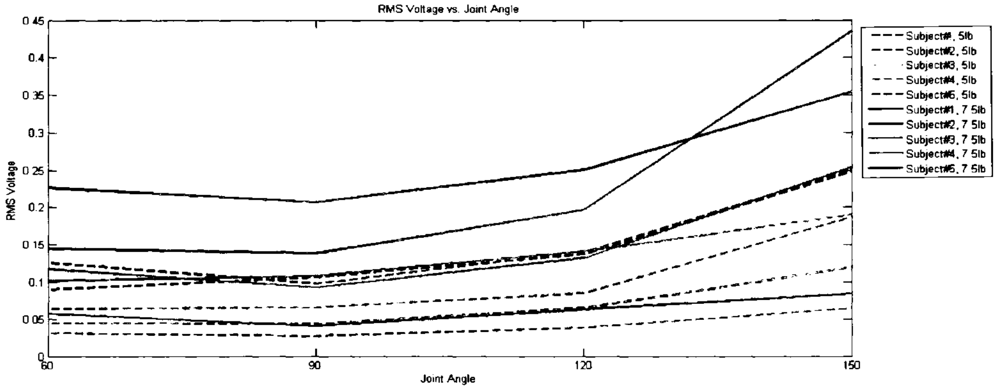

Figure 5.5: RMS voltage vs. joint angle.

Table 5.1: Average RMS voltage for different torque-joint angle combinations.

Weight	5 lb				7.5 lb			
Joint Angle	**60°**	**90°**	**120°**	**150°**	**60°**	**90°**	**120°**	**150°**
Subject#1	0.090	0.106	0.137	0.248	0.226	0.207	0.250	0.355
Subject#2	0.126	0.098	0.140	0.250	0.145	0.138	0.197	0.435
Subject#3	0.045	0.044	0.065	0.119	0.102	0.109	0.141	0.190
Subject#4	0.064	0.066	0.085	0.187	0.117	0.093	0.132	0.255
Subject#5	0.031	0.027	0.038	0.065	0.057	0.040	0.063	0.084

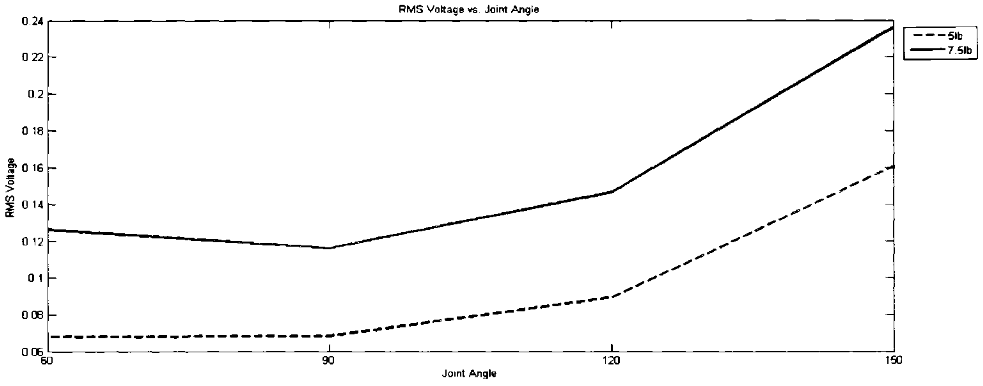

Figure 5.6: Average RMS voltage for all subjects vs. joint angle.

5.2.4.2 eFD Using Katz Method vs. Joint Angle

Figure 5.7 and table 5.2 show the eFD averaged over the three trials using Katz method versus joint angle for all subjects. The eFD averaged across all subjects follows the same trend as RMS voltage (figure 5.8). This is expected because Katz method essentially estimates the fractal dimension by length, which is strongly dependent on the amplitude of the signal (section 2.3.1). The optimal joint angle for force production is expected to happen when the joint angle is somewhere between 90° and 120°. Note that changes of eFD between different joint angles are more noticeable for lower torques in the same fashion as RMS voltage. It is hard to tell how force and depth of active MUs are individually changing the eFD.

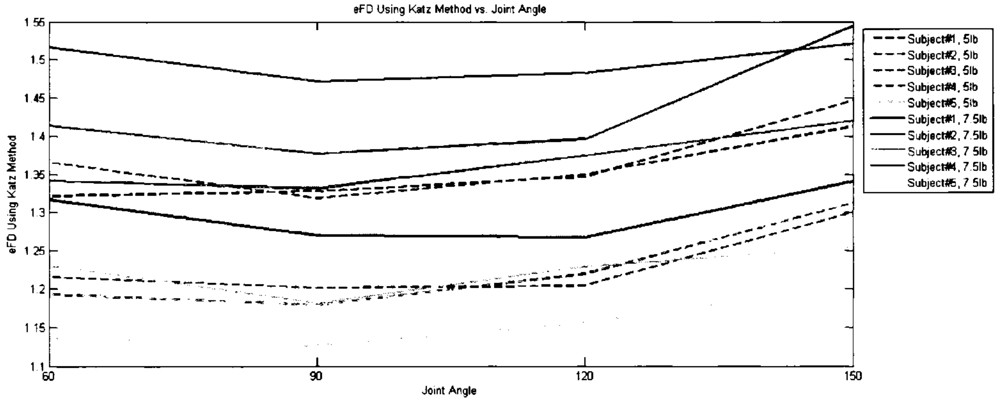

Figure 5.7: eFD using Katz method vs. joint angle.

Table 5.2: Average eFD using Katz method for different torque-joint angle combinations.

Weight	5 lb				7.5 lb			
Joint Angle	60°	90°	120°	150°	60°	90°	120°	150°
Subject#1	1.209	1.214	1.229	1.310	1.366	1.330	1.339	1.369
Subject#2	1.244	1.207	1.232	1.282	1.283	1.253	1.269	1.388
Subject#3	1.110	1.099	1.129	1.202	1.225	1.217	1.251	1.288
Subject#4	1.126	1.116	1.117	1.192	1.206	1.168	1.166	1.224
Subject#5	1.068	1.062	1.081	1.120	1.137	1.101	1.137	1.157

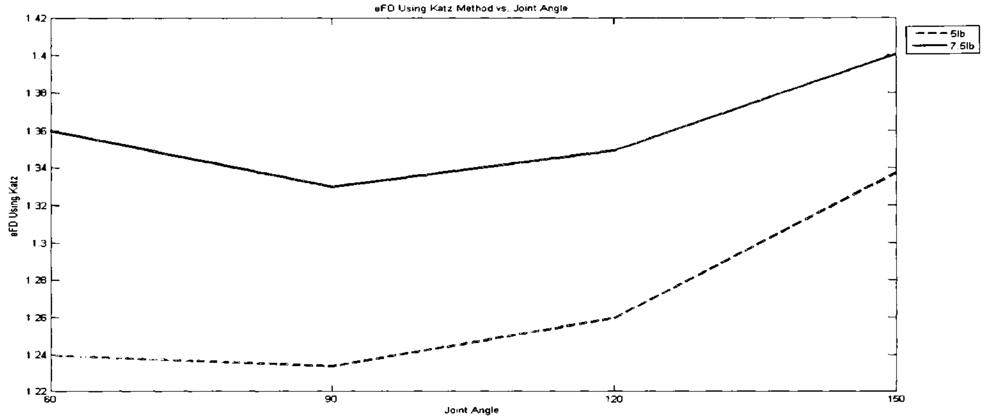

Figure 5.8: Average eFD for all subjects using Katz method vs. joint angle.

5.2.4.3 eFD Using Box-Counting Method vs. Joint Angle

Figure 5.9 and table 5.3 show the eFD averaged over the three trials using Box-Counting method versus joint angle for all subjects. Figure 5.10 show average results of all subjects. Results suffer from the saturation of the method (section 2.3.2). The eFD values remain in the 1.6 to 1.8 region and display a high degree of variation, obscuring any trends.

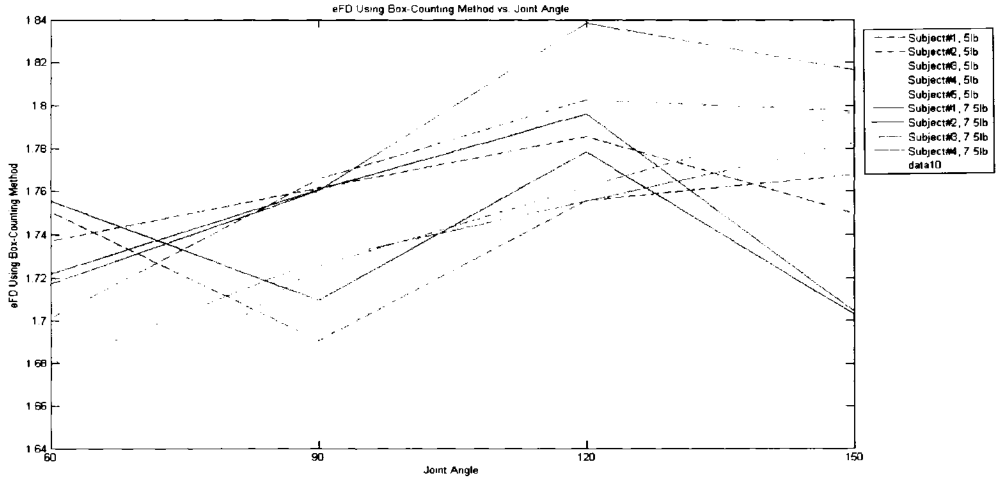

Figure 5.9: eFD using Box-Counting method vs. joint angle.

Table 5.3: Average eFD using Box-Counting method for different torque-joint angle combinations.

Weight	**5 lb**				**7.5 lb**			
Joint Angle	**60°**	**90°**	**120°**	**150°**	**60°**	**90°**	**120°**	**150°**
Subject#1	1.750	1.691	1.755	1.767	1.755	1.709	1.778	1.702
Subject#2	1.737	1.761	1.785	1.749	1.721	1.760	1.795	1.704
Subject#3	1.802	1.788	1.712	1.720	1.732	1.715	1.761	1.787
Subject#4	1.701	1.765	1.802	1.797	1.717	1.760	1.838	1.816
Subject#5	1.744	1.788	1.810	1.802	1.799	1.762	1.724	1.755

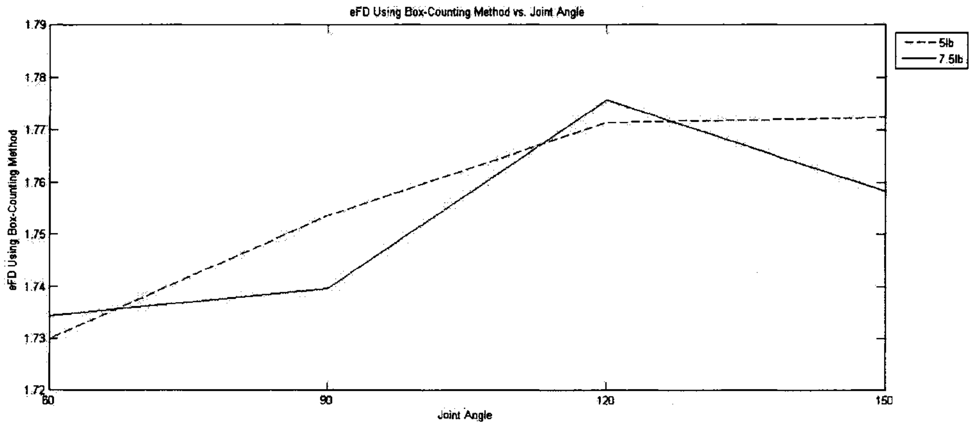

Figure 5.10: Average eFD for all subjects using Box-Counting method vs. joint angle.

5.2.4.4 eFI Using PSSM vs. Joint Angle

Applying PSSM, slope of the approximated line for the lower frequencies (left slope; α_{left}) and slope of the approximated line for the upper frequencies (right slope; α_{right}) are expected to be correlated with joint angle because they are mainly affected by depth of active MUs (section 4.3 and 4.4), which changes with joint angle. Moreover, it is expected to have the dominant effect from the joint angle not the force according to table 4.2 in section 4.4. Figure 5.11 and table 5.4 show α_{right} for each subject averaged over three trials and Figure 5.12 shows averaged results for all subjects. Figure 5.12 is consistent with the fact that α_{right} is affected mainly by joint angle and not by the number of active MUs and firing rate or in the other words effects of joint angle are dominant compared to force. Moreover it is consistent with simulated MESs and table 4.2 in section 4.4. That is, effects of depth of active MUs are larger than effects of number of active MUs and firing rate.

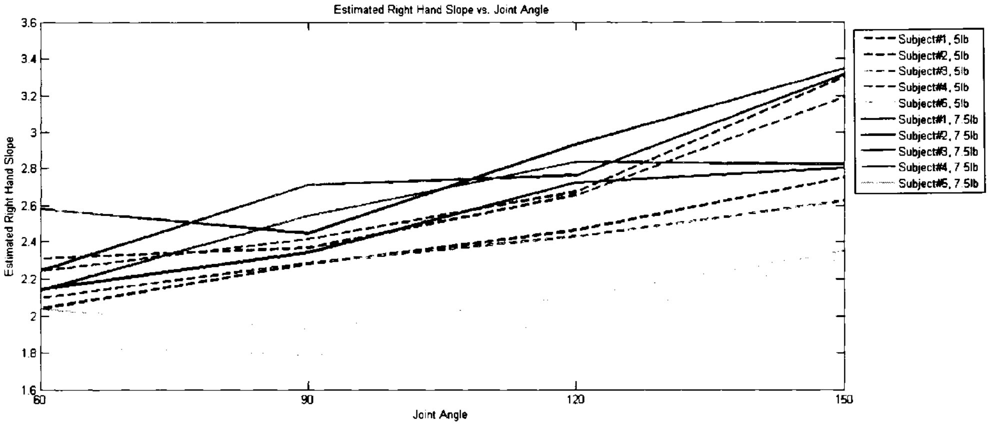

Figure 5.11: Estimated right hand slope α_{right} vs. joint angle.

Table 5.4: Average estimated right hand slope α_{right} for different torque-joint angle combinations.

Weight	**5 lb**				**7.5 lb**			
Joint Angle	**60°**	**90°**	**120°**	**150°**	**60°**	**90°**	**120°**	**150°**
Subject#1	2.033	2.260	2.460	2.738	2.130	2.310	2.702	2.788
Subject#2	2.242	2.418	2.672	3.305	2.240	2.709	2.762	3.310
Subject#3	2.096	2.285	2.432	2.622	2.130	2.542	2.826	2.818
Subject#4	2.308	2.371	2.663	3.212	2.560	2.444	2.937	3.364
Subject#5	1.833	1.781	1.976	2.311	2.036	1.927	2.100	2.348

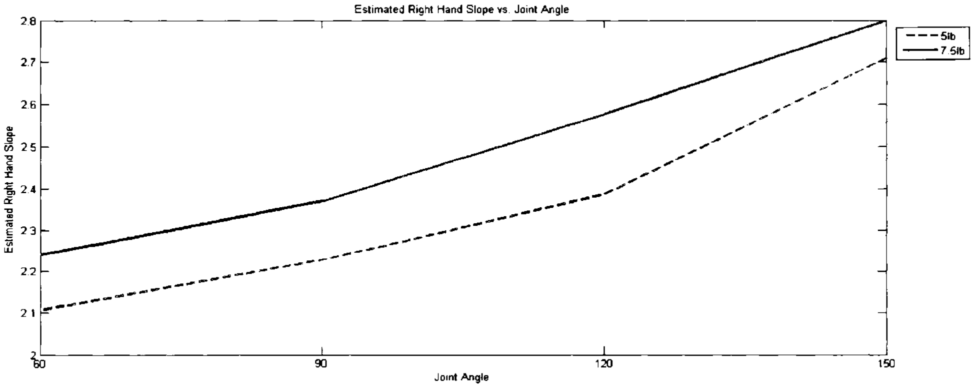

Figure 5.12: Average right hand slope α_{right} for all subjects vs. joint angle.

Figure 5.13 and table 5.5 show estimated α_{left} of each subject and Figure 5.14 average results for all subjects. Results of estimated α_{left} should a relatively consistent effect of joint angle and not by the number of active MUs and firing rate, except for one subject (subject #1); results show a decrease as the joint angle is increased . The effects of joint angle are dominant compared to effects of force, which is also consistent with the results of simulated MESs (table 4.2 in section 4.4).

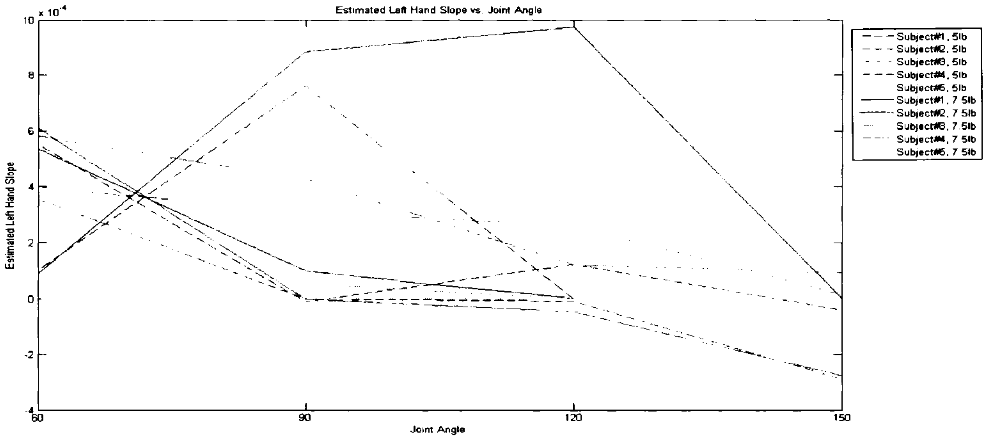

Figure 5.13: Estimated left hand slope α_{left} vs. joint angle.

Table 5.5: Average estimated left hand slope α_{left} for different torque-joint angle combinations.

Weight	**5 lb**				**7.5 lb**			
Joint Angle	**60°**	**90°**	**120°**	**150°**	**60°**	**90°**	**120°**	**150°**
Subject#1	1.02E-4	7.62E-4	0.000	0.000	8.94E-5	8.86E-4	9.75E-4	0.000
Subject#2	5.54E-4	-1.20E-5	1.21E-4	-4.1E-5	5.35E-4	9.89E-5	0.000	0.000
Subject#3	5.61E-4	9.98E-4	3.79E-4	0.000	1.05E-4	2.61E-4	9.67E-4	4.38E-4
Subject#4	4.00E-4	3.10E-4	2.61E-4	1.46E-5	5.82E-4	4.29E-4	1.19E-4	9.18E-5
Subject#5	3.57E-4	0.000	-8.90E-6	-2.9E-4	6.10E-4	0.000	-4.5E-5	-2.80E-4

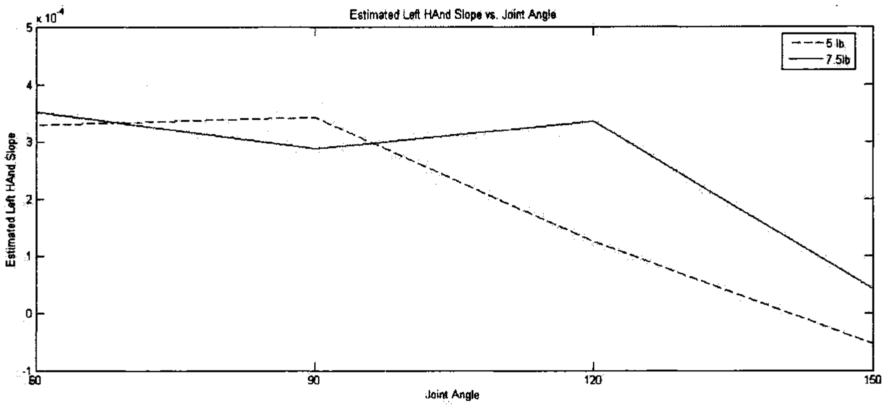

Figure 5.14: Average left hand slope α_{left} for all subjects vs. joint angle.

5.2.4.5 eFI Using GPSM vs. Joint Angle

The GPSM was also applied to the experimental data and GPSM parameters (i.e. q high frequency and g low frequency indicators) were estimated; however, a number of issues were encountered. The MES data are limited in the range of frequency points of the PSD due to the bandwidth limits of MES. As a result, the PSD only has data with points near the 'knee' or turning point of the PSD. This causes problems in convergence for the GPSM parameters estimation with standard least squares. Using a PSD estimate using the Welch method resulted in a great deal of variance in the PSD, causing further convergence problems. With the Yule-Walker method, convergence was possible for some orders (higher than 9th). While these Yule-Walker PSD estimates are perhaps not the most representative of a true MES's PSD, the results do reveal some trends.

Figure 5.15 is a plot of the PSD for subject number 1, estimated using the Yule-Walker method, with a 9th order autoregressive model and the modeled version using GPSM. This Figure shows how power spectrum shape changes as joint angle is changed. As it is illustrated in Figure 5.15 there are changes in the power spectrum at different joint angles. Another issue that causes further problems for the GPSM is the line filter that was applied to remove 60 Hz power line interference.

This method does show potential as it can generate a model for the PSD that appears to be appropriate; however, the least squares approach of parameter estimation must be replaced with another method in order to overcome the problem of convergence. A potential solution to this would be the use of an iterative least squares approach. This problem is further discussed in chapter 7.

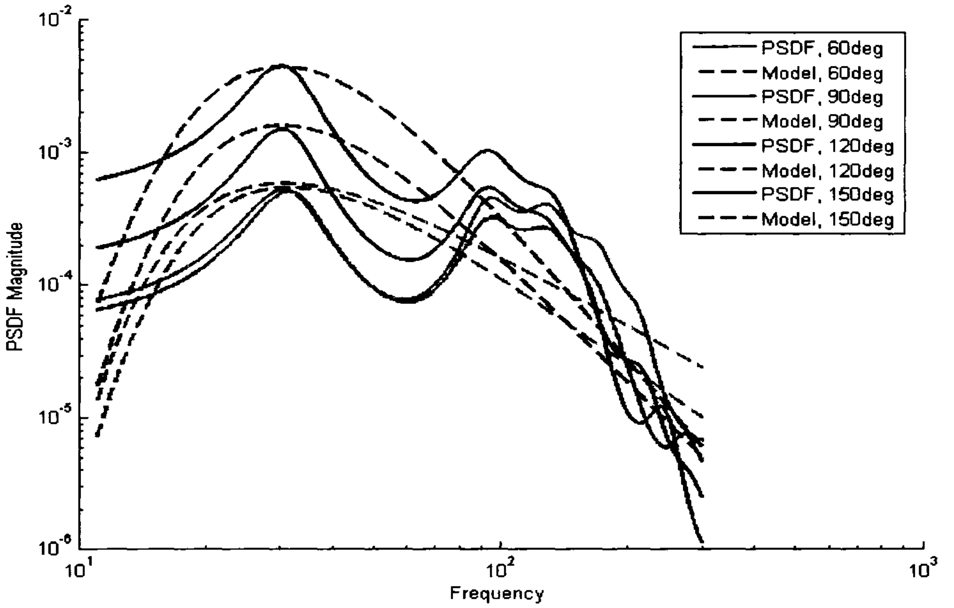

Figure 5.15: PSDF of different joint angles and their model.

5.2.5 Statistics

Table 5.9 show the quantified significance (p-values) using ANOVA which was performed in SPSS [6] for the effects of joint angle and force level on eFD using Katz method and Box-Counting method and eFI using PSSM. These values are compared to a

60° and 150° implies muscle length is closer to optimal length in these joint angles (figure 5.5). Changes are more noticeable for higher MVC levels.

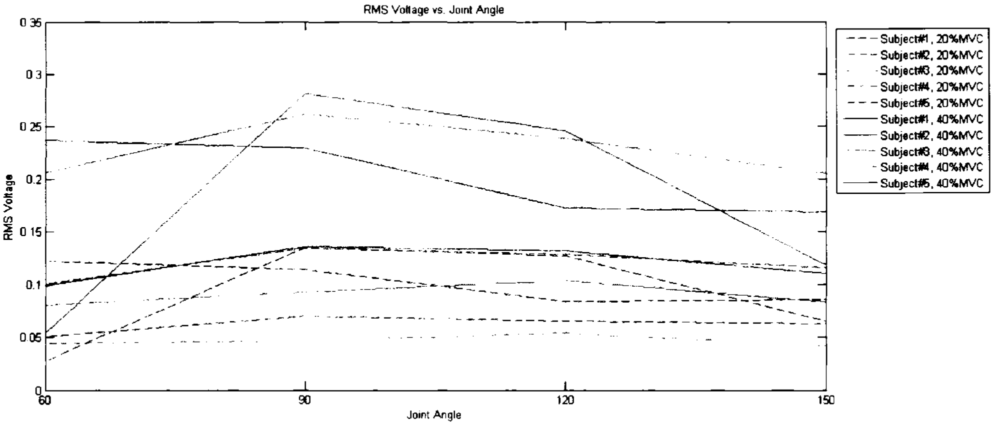

Figure 6.4: RMS voltage vs. joint angle.

Table 6.1: Average RMS voltage for different MVC level-joint angle combinations.

MVC Level	**20% MVC**				**40% MVC**			
Joint Angle	**60°**	**90°**	**120°**	**150°**	**60°**	**90°**	**120°**	**150°**
Subject#1	0.122	0.114	0.084	0.086	0.237	0.230	0.172	0.168
Subject#2	0.050	0.070	0.065	0.062	0.099	0.136	0.132	0.110
Subject#3	0.100	0.134	0.129	0.116	0.205	0.262	0.239	0.205
Subject#4	0.043	0.046	0.054	0.042	0.080	0.093	0.103	0.083
Subject#5	0.028	0.135	0.127	0.065	0.053	0.282	0.246	0.118

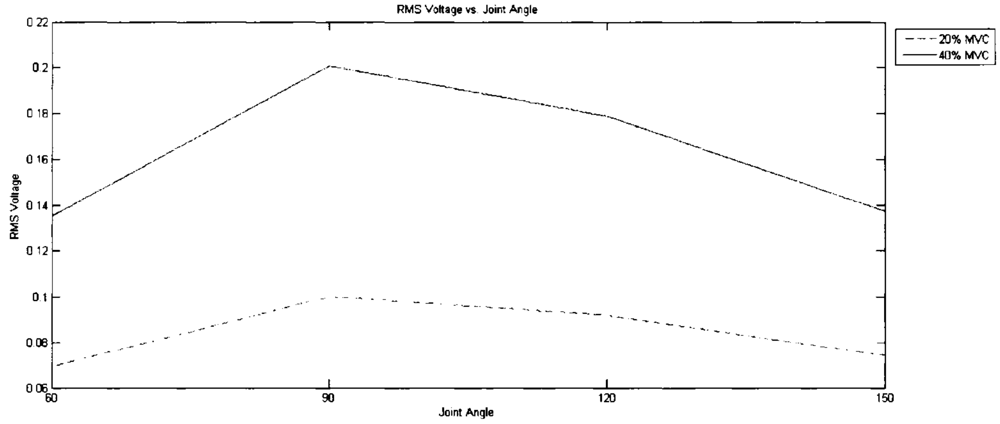

Figure 6.5: Average RMS voltage for all subjects vs. joint angle.

6.1.4.2 eFD Using Katz Method vs. Joint Angle

Figure 6.6 and table 6.2 show the eFD averaged over the three trials using Katz method versus joint angle for all subjects. The eFD averaged across all subjects follows the same trend as RMS voltage (figure 6.7). This is expected because Katz method essentially estimates the fractal dimension by signal length, which is affected by the amplitude of the signal (section 2.3.1). Changes of eFD between different joint angles are more noticeable for higher MVC levels in the same fashion as RMS voltage. As force and joint angle both cause changes in the eFD of similar magnitude, it would be difficult to distinguish either from the eFD.

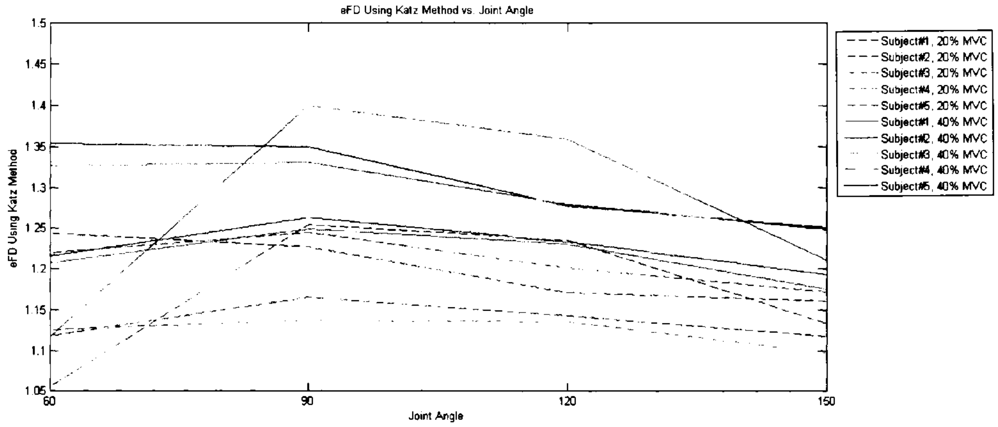

Figure 6.6: eFD using Katz method vs. joint angle.

Table 6.2: Average eFD using Katz method for different MVC level-joint angle combinations.

MVC Level	20% MVC				40% MVC			
Joint Angle	60°	90°	120°	150°	60°	90°	120°	150°
Subject#1	1.243	1.227	1.170	1.160	1.354	1.349	1.277	1.250
Subject#2	1.118	1.165	1.142	1.117	1.215	1.263	1.233	1.192
Subject#3	1.220	1.245	1.200	1.172	1.326	1.331	1.279	1.247
Subject#4	1.125	1.137	1.135	1.097	1.207	1.249	1.230	1.174
Subject#5	1.055	1.254	1.236	1.133	1.117	1.400	1.359	1.210

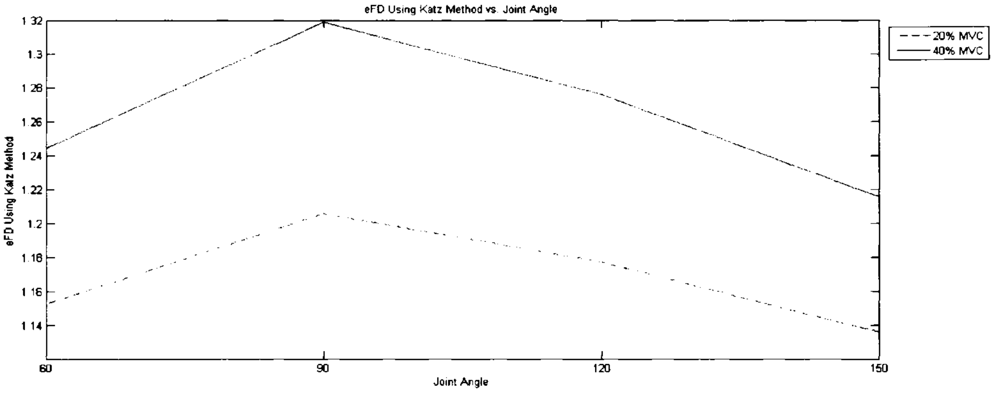

Figure 6.7: Average eFD for all subjects using Katz method vs. joint angle.

6.1.4.3 eFD Using Box-Counting Method vs. Joint Angle

Figure 6.8 and table 6.3 show the eFD averaged over the three trials using Box-Counting method versus joint angle for all subjects. Figure 6.9 show average results of all subjects. Results suffer from the saturation of the method (section 2.3.2). The eFD values remain in the 1.6 to 1.8 region and display a high degree of variation, obscuring any trends.

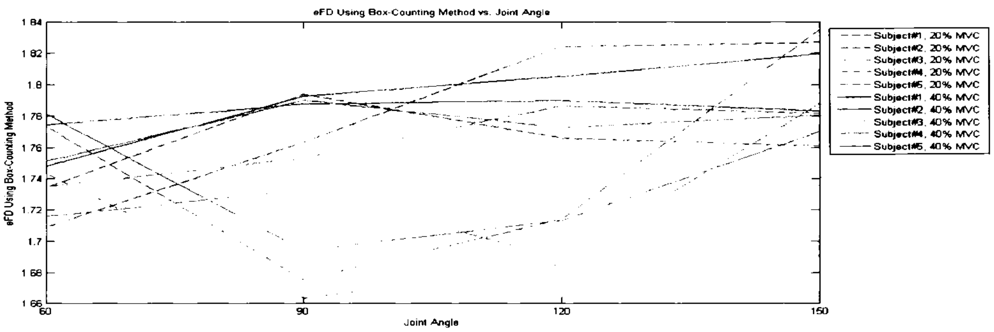

Figure 6.8: eFD using Box-Counting method vs. joint angle.

Table 6.3: Average eFD using Box-Counting method for different MVC level-joint angle combinations.

MVC Level	20% MVC				40% MVC			
Joint Angle	60°	90°	120°	150°	60°	90°	120°	150°
Subject#1	1.709	1.763	1.824	1.827	1.747	1.792	1.805	1.819
Subject#2	1.734	1.794	1.766	1.761	1.774	1.787	1.789	1.783
Subject#3	1.734	1.753	1.786	1.781	1.751	1.790	1.772	1.780
Subject#4	1.743	1.663	1.685	1.690	1.715	1.732	1.689	1.788
Subject#5	1.773	1.675	1.714	1.835	1.781	1.694	1.713	1.770

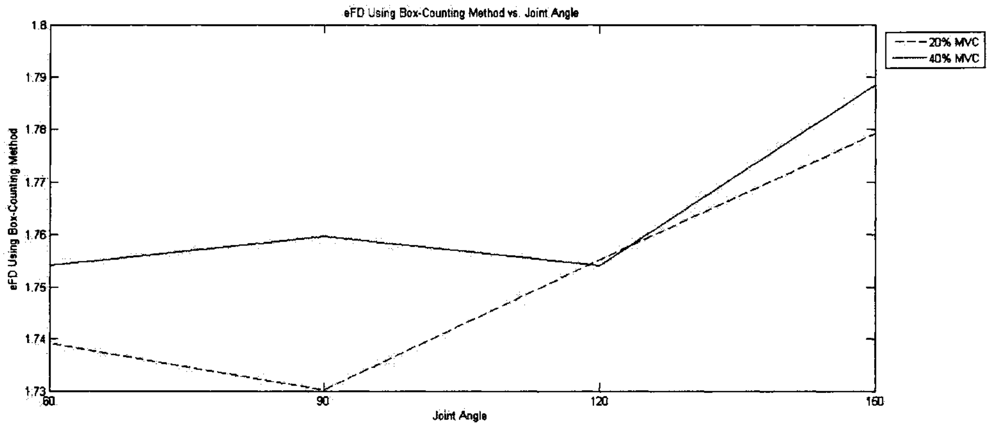

Figure 6.9: Average eFD for all subjects using Box-Counting method vs. joint angle.

6.1.4.4 eFI Using PSSM vs. Joint Angle

Applying PSSM, slope of the approximated line for the lower frequencies (left slope; α_{left}) and slope of the approximated line for the upper frequencies (right slope; α_{right}) are expected to be correlated with joint angle because they are mainly affected by depth of active MUs (section 4.3 and 4.4), which changes with joint angle. Moreover it is expected to have the dominant effect from the joint angle not the force according to table 4.2 in section 4.4. Figure 6.10 and table 6.4 show α_{right} for each subject averaged over three trials and Figure 6.11 show averaged results for all subjects. Figure 6.11 is consistent with the fact that α_{right} is affected mainly by joint angle and not by the number of active MUs and firing rate or in the other words effects of joint angle are dominant compared to force. Moreover, it is consistent with simulated MESs and table 4.2 in section 4.4. That is effect of depth of active MUs is larger than effects of number of active MUs and firing rate.

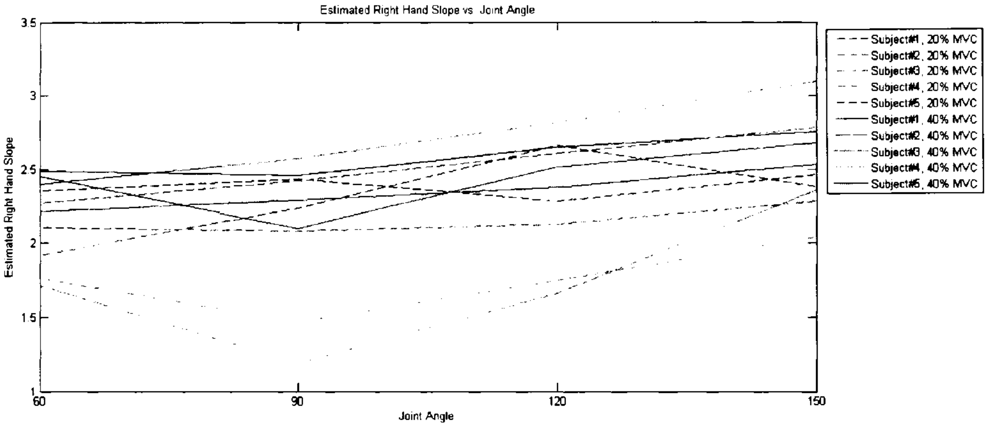

Figure 6.10: Estimated right hand slope α_{right} vs. joint angle.

Table 6.4: Average estimated right hand slope α_{right} for different MVC level-joint angle combinations.

MVC Level	**20% MVC**				**40% MVC**			
Joint Angle	**60°**	**90°**	**120°**	**150°**	**60°**	**90°**	**120°**	**150°**
Subject#1	2.349	2.433	2.279	2.463	2.485	2.457	2.645	2.750
Subject#2	2.099	2.080	2.127	2.280	2.212	2.284	2.376	2.533
Subject#3	2.270	2.424	2.607	2.779	2.396	2.572	2.814	3.096
Subject#4	1.758	1.470	1.747	2.035	1.714	1.191	1.661	2.357
Subject#5	1.915	2.235	2.662	2.378	2.448	2.093	2.515	2.677

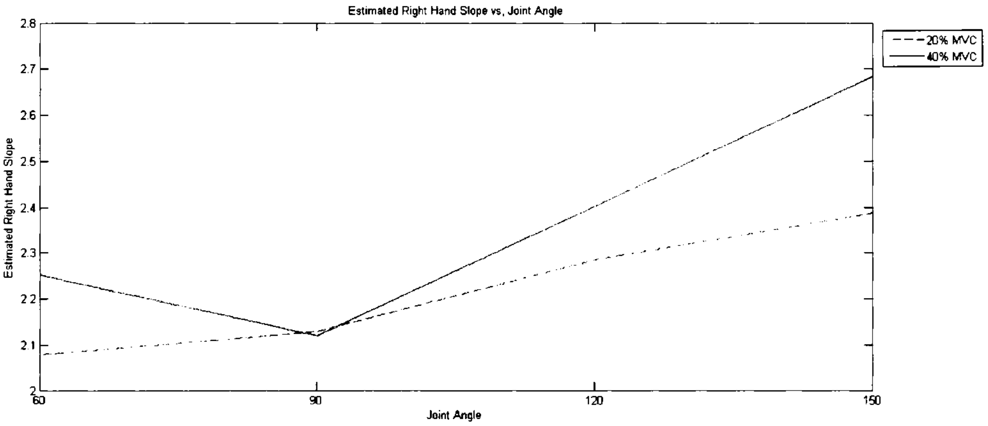

Figure 6.11: Average right hand slope α_{right} for all subjects vs. joint angle.

Figure 6.12 and table 6.5 show estimated α_{left} of each subject and Figure 6.13 average results for all subjects. Results of estimated α_{left} are affected by depth of active MUs but also by the number of active MUs and firing rate. The variance in the results do not demonstrate any significant effect of either force or joint angle.

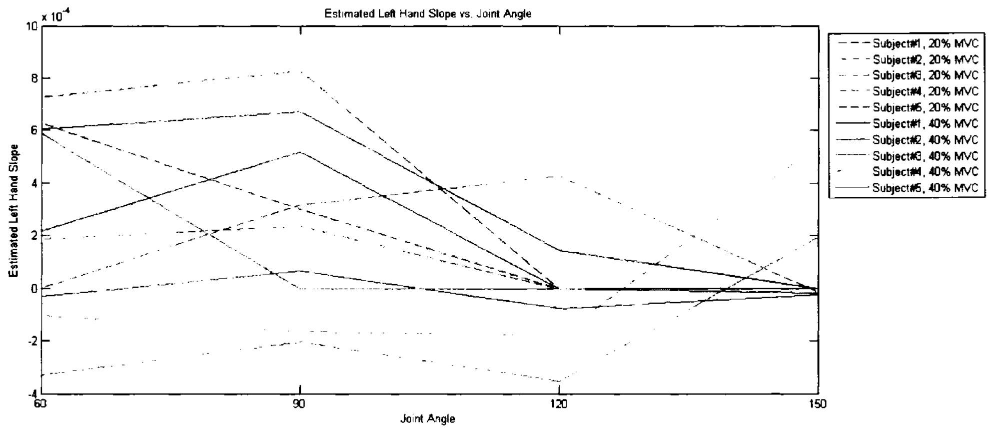

Figure 6.12: Estimated left hand slope α_{left} vs. joint angle.

Table 6.5: Average estimated left hand slope α_{left} for different MVC level-joint angle combinations.

MVC Level	**20% MVC**				**40% MVC**			
Joint Angle	**60°**	**90°**	**120°**	**150°**	**60°**	**90°**	**120°**	**150°**
Subject#1	7.28E-4	8.29E-4	0.0000	0.0000	6.05E-4	6.72E-4	1.45E-4	0.0000
Subject#2	6.27E-4	3.02E-4	0.0000	0.0000	2.16E-4	5.19E-4	0.0000	0.0000
Subject#3	1.88E-4	2.36E-4	0.0000	0.0000	5.89E-4	0.0000	0.0000	-1.90E-5
Subject#4	-1.00E-4	-1.60E-4	-1.80E-4	5.45E-4	-3.30E-4	-2.00E-4	-3.50E-4	1.94E-4
Subject#5	0.0000	3.18E-4	4.30E-4	-1.30E-5	-3.00E-5	6.56E-5	-7.50E-5	-2.30E-5

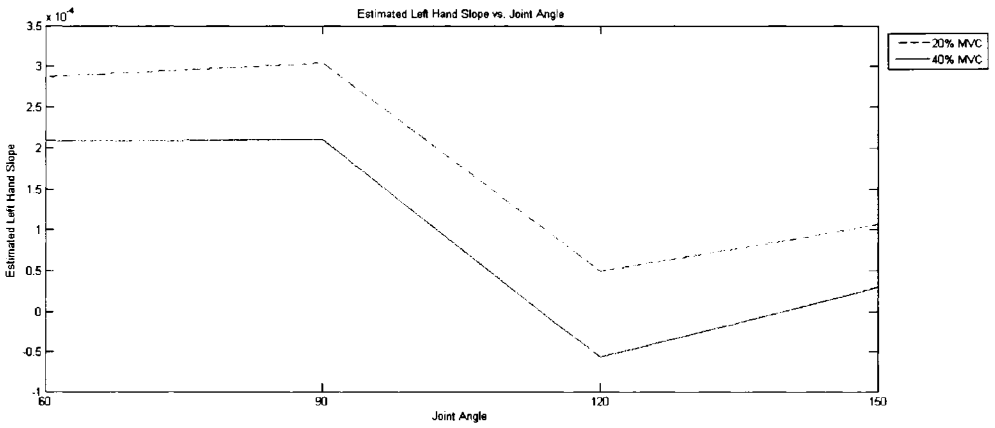

Figure 6.13: Average left hand slope α_{left} for all subjects vs. joint angle.

6.1.5 Statistics

Table 6.9 show the quantified significance (*p*-values) using ANOVA analysis which was performed in SPSS [2] for the effects of joint angle and force level on eFD using Katz method and Box-Counting method and eFI using PSSM. These values are compared to a level of significance (α=0.05). Values below this threshold show a significant effect and values higher than the threshold show insensitivity, with significance highlighted in bold.

Table 6.9: ANOVA of joint angle and force level (*p*-values with signficant effects shown in bold; α_T = 0.05) joint

Method/Parameter	Force	Joint Angle
RMS Value	**< 0.001**	0.076
Katz Method	**< 0.001**	0.091
Box-Counting Method	0.152	0.271
PSSM, Right Slope	**0.030**	**0.003**
PSSM, Left Slope	0.318	0.134

The eFD using Katz method is significantly affected by force level. Higher levels of force caused larger number of active MUs and firing rate resulted to larger amplitudes hence larger eFD's. Moreover at different joint angles recruitment and firing rate strategies are changed and again amplitude is changed hence the eFD. At different joint angles depth of the active MUs are changed too. It is hard to differentiate between the effects individually. At the joint angles where the muscle length is closer to optimal length muscle produces higher tensions or which results in a higher amplitude of the MES hence a higher eFD. This effect shows off as a shape in the same fashion like RMS voltage, which shows effects of depth of active MUs is smaller than effects caused by the number of active MUs and firing rate.

The eFD using Box-Counting method is not significantly affected by neither force nor joint angle. This is because its values remained saturated in the 1.6 to 1.8 region and display a high degree of variation, obscuring any trends.

Estimated right slope α_{right} using PSSM is significantly affected by both force level and joint angle; however changes caused by the depth of active MUs at different joint angles are larger compared to the changes imposed by the number of active MUs and their firing rates. This is also consistent with Ravier's *et al.* [3] results in which they stated that the right slope α_{right} is highly correlated with force and significantly affected by force. Estimated left slope α_{left} using PSSM is not significantly affected by neither joint angle nor the force level. High variance of the results might have caused this insensitivity.

Results from this IVC study display large variability compared to the ICFC study, which is expected in studies involving MVC. There is an increased difficulty in obtaining reliable data, including factors as the reliance of subjects using visual feedback to maintain constant force levels. Despite, the variability in the results, they demonstrate trends that appear to be consistent with what is expected. Spectral methods for computing eFI appears to be superior to eFD computed using time domain methods.

References

[1] Medical Research Council of Canada (MRC), Natural Sciences and Engineering Research Council (NSERC) of Canada, Social Sciences and Humanities Research Council (SSHRC) of Canada, *Tri-Council Policy Statement: Ethical Conduct for Research Involving Humans*, Public Works and Government Services Canada, MR21-18, 1998.

[2] www.SPSS.com

[3] P. Ravier, O. Buttelli, R. Jennane, P. Couratier, "An EMG fractal indicator having different sensitivities to changes in force and muscle fatigue during voluntary static muscle contractions," *J. Electromyography Kinesiol.*, vol. 15, pp. 210-221, 2005.

Chapter 7

Conclusions And Future Work

7.1 Conclusions

This research analyzed eFD and eFI extracted from the time domain representation of MES (i.e. Katz method and Box-Counting method) and power spectrum of the MES (i.e. PSSM and GPSM).

Firstly, an analysis was done on the simulated MESs and effects of MES's parameters (i.e. number of active MUs, firing rate and depth of active MUs) on the eFD and eFI were investigated. Results showed a significant effect of all three parameters on the Katz method and Box-Counting method, with changes in eFD caused by each parameter being of a similar magnitude.

The eFIs using PSSM and GPSM showed a greater variation due to the depth of active MUs compared to number of active MUs and firing rate. This was caused by changes in the depth of active MUs imposing changes to the power spectrum shape; meanwhile, changes in the number of active MUs and firing rate changes also causes changes in power spectrum but only small changes in the spectral slopes estimated using PSSM and GPSM's parameters compared to the changes due to MU depth. Overall, results showed that eFIs using PSSM and GPSM are significantly affected by the depth of active MUs and that they are not significantly affected by the number of active MUs and firing rate.

Secondly, eFD and eFI were analyzed during ICFC at different joint angles. It was shown that the eFIs using PSSM significantly affected joint angle and was not significantly affected by recruitment strategies. Results appear to be consistent with the simulated

MESs. The effect of joint angle on eFI, can in part be explained by changes in the measurement geometry (e.g. MU depth) for the different angles.

Thirdly, eFD and eFI were analyzed during IVC, meanwhile, the general trend seen in ICFC was also observed, and a large variation of the results caused less reliability. High variance of the results could mainly be explained due to the increased difficulty of monitoring subjects producing force during IVC.

During all of these three parts, it was shown that both Box-Counting and Katz methods for computing the eFD are heavily influenced by the amplitude of the MES, which increases as the force production increases; therefore, information delivered by this measure is not purely reflecting the complexity of the signal and there is a confusion about how much it is related to complexity and/or amplitude. However, PSSM and GPSM are superior methods of quantifying the signal complexity and they are not affected by amplitude. Meanwhile insensitivity of eFIs to force provides a possible measure for estimating the joint angle independent of recruitment strategies.

It was also shown that GPSM, using a more general model and taking in to account the whole PSD shape, provides a clearer relationship between the MES parameters and fractal geometry of the signal compared to PSSM which uses single lines for approximating the PSD. However, there are some issues that should be solved for applying GPSM to MESs.

7.2 Contributions

1. Three different methods of computing eFD and eFI (i.e. Katz method, Box-Counting method and PSM) were presented and compared using synthetic fractal signals.

2. The GPSM were introduced in the context of MESs for the first time.
3. Effects of MES's parameters (i.e. number of active MUs, firing rate and depth of active MUs) on eFD and eFI were studied using simulated MESs.
4. Effects of force and joint angle on eFD and eFI were analyzed, whereas previous works had only examined force effects.
    a. experimental study of the effects of force level and joint angle on the eFD and eFI was performed, during ICFC.
    b. experimental study of the effects of force level and joint angle on the eFD and eFI was performed, during IVC.
5. The Katz method for computing the eFD was shown to be sensitive to the signal amplitude. It was shown that this is not a suitable method for computing the eFD for time functions. For MES, the eFD is highly correlated with the RMS value, limiting the utility of this eFD.
6. The Box-Counting method for computing the eFD was shown to be sensitive to the signal amplitude too. It is not a suitable method for computing the eFD for time functions. The Box-Counting method also has a problem of saturating for time function. This method also needs a large number of samples for accurate results. For MES, the eFD is highly correlated with the RMS value, limiting the utility of this eFD and often the Box-Counting eFD was saturated, which obscured any trends.
7. The PSM for computing the eFI was shown to be a direct and effective method. In the case of MESs, PSSM provides eFIs independent of recruitment strategies and RMS value, while highly correlated with depth of active MUs and joint angle.

8. The GPSM is expected to have a similar performance to the PSSM as the g and q parameters characterize the spectral slopes of the PSD; however, practical use of the GPSM was problematic because of the variability in the PSD estimate and data limited to the "knee" of the model which caused the method to diverge. Moreover, the GPSM couples parameter g with the high frequency behavior and high and low frequency indicators are not independent.

7.3 Future Work

1. The eFD and eFI during IVC should be further analyzed with a larger number of subjects. To reduce the variance of the results a larger subject pool should be provided and also a more sophisticated training protocol introduced. Measuring 100% MVC is also a critical stage that must be further investigated.
2. Standard least squares used in GPSM is not a suitable approach for MESs. For example, GPSM would not converge using estimated PSD with Welch method. Different approaches to model parameter estimation such as an iterative least squares approach should be considered instead.
3. An adaptive filtering of 60 Hz noise should be considered instead of notch filtering to eliminate the dip in current data.
4. A modification to the general model of GPSM, as shown in Eqn 7.1 could be a possible way for decoupling the effect parameter g has on the high frequency behavior of the model. This new model should be further investigated as well.

$$P(k)=\frac{c\left|k/k_0\right|^{2g}}{\left(\left(k/k_0\right)^2+1\right)^{q+g}} \qquad 7.1$$

References

[1] P. Ravier, O. Buttelli, R. Jennane, P. Couratier, "An EMG fractal indicator having different sensitivities to changes in force and muscle fatigue during voluntary static muscle contractions," *J. Electromyography Kinesiol.*, vol. 15, pp. 210-221, 2005.

Appendix A

Solution of $\frac{d^q}{dx^q} f(x) = n(x)$, is self affine.

Proof

By definition,

$$\frac{d^q}{dx^q} f(x) = \frac{1}{2\pi} \int_{-\infty}^{\infty} (ik)^q F(k) \exp(ikx) dk \qquad \text{A.1}$$

where $F(k)$ is the Fourier transform of $f(x)$, given by

$$F(k) = \int_{-\infty}^{\infty} f(x) \exp(-ikx) dx \qquad \text{A.2}$$

where k is the spatial frequency. Using A.1 and A.2, $\frac{d^q}{dx^q} f(x) = n(x)$ can be rewritten as,

$$f(x) = \frac{1}{2\pi} \int_{-\infty}^{\infty} \frac{1}{(ik)^q} N(k) \exp(ikx) dk \qquad \text{A.3}$$

where $N(k)$ is the Fourier transform of the $n(x)$. Using convolution theorem,

$$f(x) = \int h(x-y) n(y) dy \qquad \text{A.4}$$

Defining $h(x)$ as,

$$h(x) = \frac{1}{2\pi} \int_{-\infty}^{\infty} \frac{\exp(ikx)}{(ik)^q} dk \qquad \text{A.5}$$

Substituting p for ik, $h(x)$ can be rewritten in terms of the inverse Laplace transform of p^{-q}.

$$\hat{L}[x^q] = \frac{\Gamma(q+1)}{p^{q+1}} \qquad \text{A.6}$$

where $\hat{L}$ denotes the Laplace transform and Γ is the Gamma function,

$$\Gamma(q) = \int_0^\infty t^{q-1} \exp(-t) dt \qquad \text{A.7}$$

$$\hat{L}[x^q] = \frac{\Gamma(q+1)}{p^{q+1}} \Rightarrow x^q = \hat{L}^{-1}\left[\frac{\Gamma(q+1)}{p^{q+1}}\right] \qquad \text{A.8}$$

or,

$$\hat{L}^{-1}\left[\frac{1}{p^q}\right] = \frac{1}{\Gamma(q)} x^{q-1} \qquad \text{A.9}$$

This leads to Liouville-Riemann transform, an example of fractional integral. This transform is consistent with the statistical self affinity. Consider,

$$f'(x) = \frac{1}{\Gamma(q)} \int_0^x \frac{n(\lambda y)}{(x-y)^{1-q}} dy \qquad \text{A.10}$$

substituting $z = \lambda y$,

$$f_\lambda(x) = \frac{1}{\lambda^q} \frac{1}{\Gamma(q)} \int_0^{\lambda x} \frac{n(z)}{(\lambda x - z)^{1-q}} dz = \frac{1}{\lambda^q} f(\lambda x) \qquad \text{A.11}$$

As long as $f(\lambda x)$ and $f_\lambda(x)$ are stochastic processes, A.11 means,

$$\Pr\{f_\lambda(x)\} = \lambda^{-\alpha} \Pr\{f(\lambda x)\} \qquad \text{A.12}$$

which describes a statistical self affine signal.

Appendix B

A signal f with power spectrum $P(k)=\frac{c|k|^{2g}}{(k_0{}^2+k^2)^q}$ is self affine.

Proof

Writing complex spectrum of f in form of Eqn B.1,

$$F(k)=H(k)N(k) \qquad \text{B.1}$$

where $N(k)$ is the complex spectrum of white noise and $H(k)$ is the transfer function,

$$H(k)=\frac{(ik)^g}{(k_0+ik)^q} \qquad \text{B.2}$$

f is then given by,

$$f(x)=\frac{1}{2\pi}\int_{-\infty}^{+\infty}H(k)N(k)\exp(ikx)dk \qquad \text{B.3}$$

Using convolution theorem B.3 can be written as,

$$f(x)=\int h(x-y)\frac{d^g}{dy^g}n(y)dy \qquad \text{B.4}$$

where

$$h(x)=\frac{1}{2\pi}\int_{-\infty}^{+\infty}\frac{1}{(k_0+ik)^q}\exp(ikx)dk \qquad \text{B.5}$$

Substituting p for ik, B.5 can be written in form of a inverse Laplace transform,

$$h(x)=\hat{L}^{-1}\left[\frac{1}{(k_0+p)^q}\right] \qquad \text{B.6}$$

Since

$$\hat{L}\left[x^q\exp(-k_0x)\right]=\frac{\Gamma(q+1)}{(k_0+p)^{q+1}},\ q>-1,\ Re(p+k_0)>0 \qquad \textit{B.7}$$

it follows that,

$$h(x)=\frac{1}{\Gamma(q)}\frac{\exp(-ik_0x)}{x^{1-q}} \qquad B.8$$

Hence, f can be written as a fractional integral transform,

$$f(x)=\frac{1}{\Gamma(q)}\int_{-\infty}^{x}\frac{\exp\left[-k_0(x-y)\right]}{(x-y)^{1-q}}\frac{d^g}{dy^g}n(y)dy \qquad \text{B.9}$$

Considering B.10,

$$\begin{aligned}f'(x;k_0)&=\frac{1}{\Gamma(q)}\int_{-\infty}^{x}\frac{\exp\left[-k_0(x-y)\right]}{(x-y)^{1-q}}\frac{d^g}{dy^g}n(\lambda y)dy\\&=\frac{\lambda^g}{\lambda^q}\frac{1}{\Gamma(q)}\int_{-\infty}^{\lambda x}\frac{\exp\left[-\frac{k_0}{\lambda}(\lambda x-z)\right]}{(\lambda x-z)^{1-q}}\frac{d^g}{dz^g}n(z)dz \qquad \text{B.10}\\&=\frac{\lambda^g}{\lambda^q}f(\lambda x;{}^{k_0}\!/\!_{\lambda})\end{aligned}$$

Hence the scaling relationship for this model is B.11 and it is consistent with definition of self affinity,

$$\Pr\left[f'(x,k_0)\right]=\frac{\lambda^g}{\lambda^q}\Pr\left[f(\lambda x,{}^{k_0}\!/\!_{\lambda})\right] \qquad \text{B.11}$$

Here as x is scaled by λ, the characteristic frequency k_0 is scaled by ${}^{1}\!/\!_{\lambda}$. This means zooming into the signal f the distribution of amplitudes (i.e. the probability density functions) remains the same.

Appendix C

Biological Signal Research
Carleton University
Department of Systems and Computer Engineering

INFORMED CONSENT

I, ______________________________ have been invited by Dr. Adrian Chan, and his research associates, of the Department of Systems and Computer Engineering at Carleton University, Ottawa, ON to participate in a study on biological signals.

The purpose of the study is to examine various biological signals including: electrocardiogram (ECG) – heart signal, myoelectric signal (MES) – muscle signals, electroneurogram (ENG) – nerve signals, and electroencephalogram (EEG) – brain signals.

These signals will be monitored non-invasively using electrodes on the skin surface. Although this is a non-invasive measuring technique, these surface signals contain valuable information pertaining to the status of internal organs (e.g. heart, muscles, and nerves).

I understand that surface electrodes will be placed on me to acquire the necessary biological signals. Depending on the study, the number and exact placement of the electrodes will vary. A maximum of 8 simultaneous channels will be used.

☐ **I have been fully informed of the study that I am participating in.**

Given the range of experiments I understand that I am being asked to participate in:

☐ neuromuscular study that requires the application of surface electrodes.

I may be asked some questions to ascertain some additional data, which may include: age, sex, height, weight, native language, birth place, whether I have any known neuromuscular disorders

I have been informed in advance that the study session for the data collections will be:

- ☐ approximately one hour
- ☐ up to three hours.

I may be asked to return for additional sessions, and will be informed of this at the end of the study session. I am in no way obligated to participate in these additional sessions.

There are no direct benefits or remuneration for my participation in this study.

Should the experimenter note any unusual readings during the course of the experiment the study will be stopped immediately. The experimenter is not a physician and cannot make a medical diagnosis. I will be asked to contact my family physician. The researcher will contact my physician in writing explaining why the experiment was stopped. I may not return to the study or undertake any further experiments without the written consent of my physician.

I understand that the data from this research will be used in scientific reports, presentations, and publications and my identity will remain confidential. Data will be kept electronically and my consent forms and information will be kept as a hardcopy. Access to the data will be restricted to the researcher investigators. Data may be kept for an indefinite period of time. Note data may be shared with other investigators (possibly at other institutions) for research purposes.

My identity will be kept strictly confidential unless otherwise discussed with the researcher. Any scientific report, presentation, or publication of the data will refer to me using a subject number. Information on my sex, age, and native language may be used.

Participation in this study is strictly voluntary. I am free to withdraw from the experiment at any time and without any consequences. I will also declare if the researcher can/cannot use the data I have provided should I decide to withdraw from the study.

This study has been reviewed and received ethics clearance though the Carleton University Research Ethics Committee in accordance to the Tri-Council Policy Statement for Ethical Conduct for Research Involving Humans. Should I have any concerns or questions about my involvement in this study I may contact the committee chair:
Professor Klaus Pohle, Chair
Research Ethics Committee
613-520-2600 ext. 7434
klaus_pohle@carleton.ca).

I may contact one of the investigators for consultation of any concerns I have about the research. In addition, I may also request any publications and information about the final results or conclusions from the study:
Dr. Adrian Chan
Department of Systems and Computer Engineering
Carleton University
1125 Colonel By Drive
Ottawa ON K1S 5B6 CANADA
(613) 520-2600 ext. 1535

Signature: ______________________ Date: ____________

Experimenter: ____________________ Signature: ______________________

Date: ____________

____

Research undertaken as part of a graduate or undergraduate course requirement: YES / NO

If YES specify course name and course number

____

Research undertaken as part of a graduate or undergraduate thesis research: YES / NO